Chapter 2
Optical Properties of Semiconductor Nanorods

2.1 Introduction

The optical properties of nanocrystals are dictated by their electronic structure, and we start this section with discussing the behavior of electron–hole pairs, the so called excitons, in confined systems. We then describe the optical peculiarities of semiconductor nanorods by highlighting the main characteristics that distinguish them from the more traditional quantum dots. The first part of this section will focus on the comprehension of the general properties of nanorods made of a single material (henceforth referred to as "homo-structures"), while in the second part of the section we will highlight the properties of nanorods made of sections of different materials (henceforth referred to as "heterostructures"), which have been synthesized by various groups thanks to the latest developments in colloidal nanocrystal synthesis.

2.2 Excitons and Quantum Confinement Regimes

The energy gap of a semiconductor is the energetic separation between the lowest unoccupied electronic state and the highest occupied state at 0 K. The exciton band gap is written as:

$$E_g = E_{g0} + E_q + E_C \tag{2.1}$$

where E_{g0} is the energy gap of the corresponding bulk solid, E_q is the contribution introduced by the quantization and corresponds to the zero-point energy for each system, and E_C is the contribution of the Coulomb attraction between electrons and holes. Their relative contribution is basically related to the degree of confinement to which a system is subjected. In order to better define the role of the quantum confinement on each term of the above expression, we need to introduce the concept of "exciton", which is a "quasi-particle". An exciton is a bound system, composed of an electron (e) and a hole (h) that experience a mutual Coulomb

R. Krahne et al., *Physical Properties of Nanorods*,
NanoScience and Technology, DOI: 10.1007/978-3-642-36430-3_2,

interaction. Here, we will be dealing with a particular type of exciton, in which the e–h distance is much larger than the lattice constant of the crystal in which it is formed, and is usually referred to as a "Wannier-Mott exciton" [1]. One key parameter associated with the exciton is its binding energy, which is defined as:

$$E_b = \frac{\hbar^2}{2\mu r_B^2} \tag{2.2}$$

In the expression above, μ is the reduced mass of the exciton, defined as $1/\mu = (1/m_e + 1/m_h)$, m_e and m_h being the effective masses of electrons and holes, respectively. r_B represents instead the Bohr radius of the exciton, defined as:

$$r_B = \frac{\hbar^2 \varepsilon^2}{\mu e^2} \tag{2.3}$$

with ε being the dielectric constant of the semiconductor. The Bohr radius of the exciton represents its natural spatial extension after its creation (i.e. upon electron–hole pair generation) until its annihilation (upon electron–hole recombination). In bulk semiconductors such radius ranges from a few nm to some tens of nm, depending on the material. The quantization energy is related to the zero-point energy of electrons and holes in the system, and it has always a positive value. In a spherical nanocrystal, for instance, it is defined as [2]:

$$E_q^{e,h} = \frac{\hbar^2 \pi^2}{2m_{e,h} a^2} \tag{2.4}$$

The Coulomb contribution is in general negative, but in some cases it can also be positive (see later in this section). It is proportional to $e^2/\varepsilon^2 a$ and in a spherical quantum dot it can be estimated (as a first approximation) as being equal to [2]:

$$E_C = -1.8 \frac{e^2}{\varepsilon^2 a} \tag{2.5}$$

Therefore, by considering all contributions, the energy gap can be derived from the following expression:

$$E_g = E_{g0} + \frac{\hbar^2 \pi^2}{2m_e a^2} + \frac{\hbar^2 \pi^2}{2m_h a^2} - 1.8 \frac{\hbar^2}{\mu r_B a} \tag{2.6}$$

The optical properties of a semiconductor nanocrystal are dictated by the ratio between the spatial confinement, i.e. the size of the nanocrystal (a), and the Bohr radius r_B of the exciton. Depending on this ratio, three different regimes of quantization can be defined: weak ($a \gg r_B$), intermediate ($a \approx r_B$) and strong ($a < r_B$). In the weak confinement regime, the Coulomb term dominates. Electrons and holes can form the exciton and do not actually "feel" the "restricted" size of the semiconductor. In the intermediate regime, the system can behave in different ways, depending on the ratios between a and the Bohr radii of electrons (r_e) and of the holes (r_h), respectively. In the case that r_h is smaller than r_e the hole will stay

confined at the center of the nanocrystal with the electron orbiting around it, similarly to the case of a donor impurity [3, 4], if a falls in between r_h and r_e. In the strong confinement regime the quantization term dominates over the binding energy of exciton.

2.3 Optical Properties of Nanorods: Overview

The dependence of the energy gap on the size of the nanocrystals is used as a powerful tool for designing materials with well-controlled optical properties. The continuous progress in the development of novel and sophisticated synthesis techniques has opened the possibility to exploit other key parameters for engineering the electronic structure of nanocrystals, such as the shape and the chemical composition. In this respect chemical approaches employing the so-called "high-temperature" thermal reaction of precursors in surfactants have become a popular route to colloidal nanoparticles. This method is so powerful and versatile that a large fraction of nanocrystals discussed in this review have been fabricated in this way. It is also important to note that this method, as many others, yields nanocrystals that are stabilized in the liquid phase by means of a monolayer of organic molecules (i.e. the surfactants) bound to their surface. These molecules need to be considered as a fundamental component of the nanocrystal as they play an important roles in the various physical properties of the nanocrystal, as will be discussed extensively in this review.

Elongated (i.e. rod-shaped) nanocrystals, also known as nanorods, are probably the most studied nanocrystal systems after the spherical ones. Other more complex shapes have been investigated too, but they will not be discussed here [5]. The typical lengths of the nanorods span from tens to some hundreds of nm, while their diameters are generally in the range of a few nm. These nanorods can be considered as intermediate systems between quantum dots and nanowires, since the nanorod length is typically larger than the Bohr radius. Therefore the carriers experience strong confinement only along two dimensions, whereas they can delocalize along the long axis of the rod, giving rise to the so called 1D exciton [6]. This confinement leads to a variety of new properties with respect to spherical nanocrystals, in terms of electronic structure, symmetry, polarization and carrier dynamics.

2.4 Electronic Structure of CdSe Nanorods: A Case Study

Among rod-shaped semiconductor nanocrystals, CdSe nanorods represent probably the most investigated samples, for what concerns both their optical and their electronic properties. Here, we will give an overview of their electronic structure, by highlighting some of the pioneering works in the field (for example those by

Efros et al. [7–9] and by Woggon et al. [10–13]). The concepts discussed here can be considered as of general validity for nanocrystals having hexagonal crystallographic structure and are applicable to nanorods of a wide range diameters and lengths. The starting point is to consider a nanocrystal with dimensions that are much greater than its lattice constant, such that the effective mass approximation [7] is applicable. This condition is practically fulfilled in all cases, since the nanocrystal diameter is hardly smaller than 2–3 nm. In the case of quantum dots, the notation used to name the quantum states follows closely that of an atomic system. We define the total angular momentum J = (L + S) as the sum of the total orbital angular momentum L and the multiplicity term S, the latter accounting for the electron spin. The relative momentum projections are j, l, and s. The electron ground state has s-symmetry and presents a double degeneracy, which is due exclusively to the spin momentum. Thus J = 0 + 1/2, its projections are j = ±1/2, and the state is conventionally indicated as $1S_e$. On the other hand, the first hole level, having a p-symmetry, is fourfold degenerate, having J = 1 + 1/2 = 3/2 (j = 3/2, 1/2, −1/2, −3/2), and is named $1S_{3/2}$. The composition of the two ground states yields the eightfold degenerate exciton ground state $1S_{3/2}1S_e$.

Various effects intervene to lift the degeneracy of the states, namely the internal crystal field, shape effects and the electron–hole exchange interaction. The first effect arises from an intrinsic property of semiconductors that have hexagonal lattice structure and therefore manifests itself in both bulk and nanoscale materials. The second effect results from the deviation from the ideal spherical shape of nanocrystals, while the third accounts for mixing of electron and hole spins. The first two effects can be grouped together, as they arise from the intrinsic asymmetry of the material/nanocrystal (see Fig. 2.1). The intrinsic crystal field produces a first splitting of the valence band, i.e. the lowest hole state, in the so called Kramers doublet, which consists of two doubly degenerate states with j = ±1/2 and j = ±3/2 [7]. Let us define a parameter β as the ratio between the mass of the light hole m_{lh} and the mass of the heavy hole m_{hh} (hence $\beta = m_{lh}/m_{hh}$). The energetic splitting due to the intrinsic crystal field is then expressed as [7]:

$$\Delta_1 = \Delta_{CF} f(\beta) \tag{2.7}$$

where Δ_{CF} is a parameter related to the crystal field (CF) splitting in a crystal with hexagonal structure, contributing to determine the hole ground state as that having |j| = 3/2, while $f(\beta)$ is a function which is unique for each material (see Ref. [7] for details). It is worth to stress that Δ_1 does not depend on the size of nanocrystal. Since $f(\beta)$ is always positive, the lowest hole level is fixed with the heavy-hole state with |j| = 3/2.

In order to take the shape anisotropy into account, let us model an elongated nanocrystal as an axially symmetric ellipsoidal particle (i.e. an ellipsoid with principal axes $a = b < c$), and let us define the ratio of the major to minor axes as $c/b = 1 + \varepsilon$, ε being the ellipticity. The induced splitting in this case is:

$$\Delta_2 = 2u(\beta)E_1(\beta)\varepsilon \tag{2.8}$$

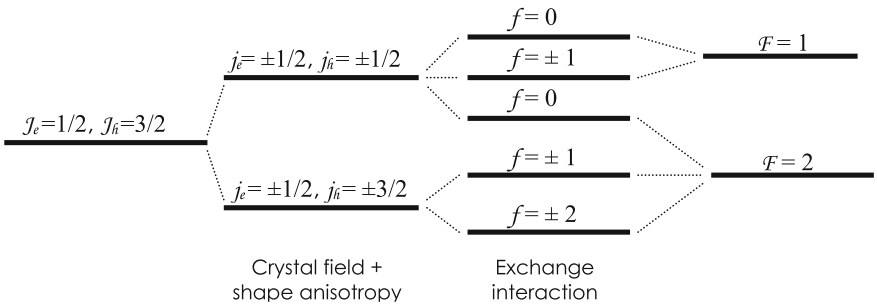

Fig. 2.1 Fine structure splitting of the lowest excitonic states $F = 1$ and $F = 2$ in CdSe nanocrystals due to crystal field, shape anisotropy and exchange interactions

Here, $u(\beta)$ is a dimensionless function associated with the hole-level splitting due to the crystal shape (see Fig. 2.2), for details see Ref. [7]) and $E_1(\beta)$ is the hole ground state energy which can be written as:

$$E_1(\beta) = \frac{\hbar^2 \varphi^2(\beta)}{2m_{hh}a^2} \tag{2.9}$$

where $\varphi^2(\beta)$ is a term related to the spherical Bessel functions and a is related to the nanocrystal size. For quasi spherical nanocrystals $a = (b^2c)^{1/3}$.

Another important point is the trend in the function $u(\beta)$, in particular for what concerns its sign [7]. As shown in Fig. 2.2c $u(\beta)$, reverses its sign past a certain value of β, meaning that for some materials the shape anisotropy induces a negative splitting. Since the global energy splitting is the sum of the single asymmetry contributions $(\Delta_t = \Delta_1 + \Delta_2)$, the final result can reverse the hole ground state between |j| = 3/2 and |j| = 1/2. A negative Δ_2 is found for example in CdSe nanorods, for which $\beta = 0.28$, and where a possible inversion would depend on the hole ground state energy and on the radius of rods.

We now discuss the excitons, formed by composition of these electron–hole states, which result in two-excitonic fourfold degenerate states, having total angular momentum F = 1 and F = 2 (see right side of Fig. 2.1). The exchange interaction contributes to an increase of the splitting of the remaining states, defining a fine structure for nanocrystals for a series of possible shapes, as depicted in Fig. 2.3 [7].

The relevant quantum number, in this case, is the projection f of the total angular momentum F. The fine structure of the lowest excitonic level is composed by a distribution of states having different values of f: one state with f = ±2, two states with f = ±1 (named Upper and Lower, depending on the branch they originate) and two others with f = 0 (Upper and Lower). Only three of them are optically active, namely the states 0^U, $\pm 1^U$ and $\pm 1^L$, whereas the remaining ±2 and 0^L states are passive [7]. The ±2 state is optically forbidden because photons cannot have an angular momentum ±2. The 0^L has zero optical transition probability because of an interference phenomenon between the two indistinguishable states

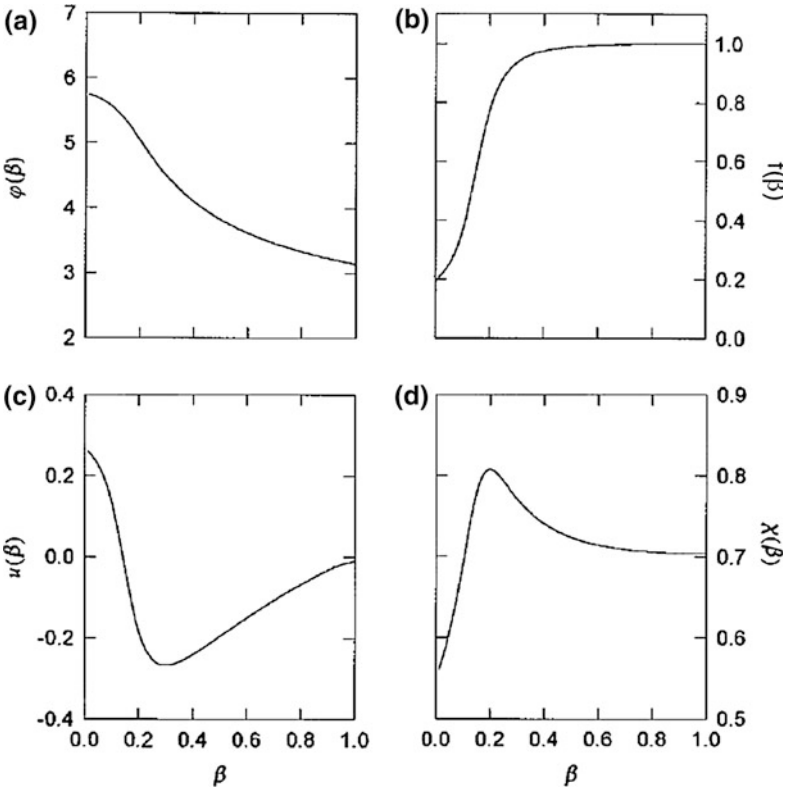

Fig. 2.2 **a** Dependence of the hole ground state function on the light-to-heavy hole ratio mass β. **b–d** Dimensionless functions associated with: **b** hole level splitting due to hexagonal lattice structure, **c** the hole splitting due to the crystal shape asymmetry, **d** the exciton splitting due to the electron–hole-interaction. Taken with permission from Ref. [7]

with zero angular momentum [2], due to the influence of the electron–hole exchange interaction.

The shape of the nanocrystal can have significant influence on which of the above states represents the exciton ground state. For perfectly spherical nanocrystals the ± 2 is the ground state, whereas in prolate nanocrystals an inversion of the ± 2 with the 0^L state can occur, because the state ± 2 originates from the hole state with $|j| = 3/2$, whilst 0^L arises from the state $|j| = 1/2$. When the conditions for the sign change of Δ_t are met, the ground state is inverted. Nanorods can be approximated by axially symmetric prolate ellipsoids with ellipticity ε defined as $\varepsilon = (2r_B/b) - 1$, with b being the ellipsoid diameter and r_B the Bohr radius. In the case of strong lateral confinement $(b < 2r_B)$, the ellipsoids are subject to a possible inversion of the ground state between $\pm$ 2 and 0^L. Following Eq. (2.8), the shape asymmetry can lead to a negative splitting value Δ_2 and then to a negative net splitting $\Delta_t = \Delta_1 + \Delta_2 < 0$, if the ellipsoid radius is smaller than a critical value.

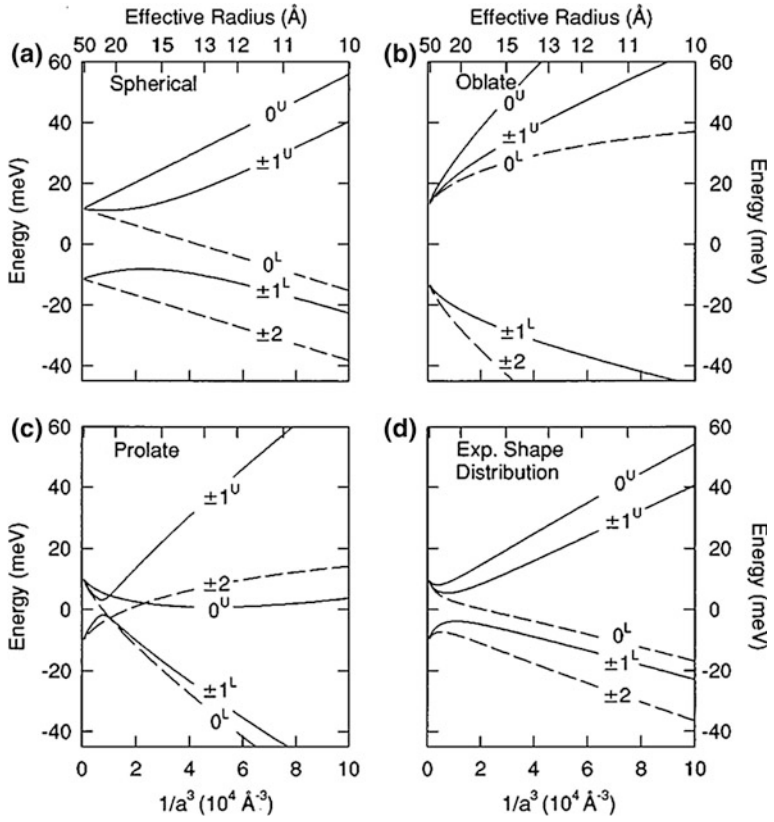

Fig. 2.3 Evolution of the band-edge exciton as a function of the nanocrystal size calculated for four different shapes. Reprinted with permission from Ref. [7]

This can happen because Δ_2 becomes increasingly important in the strong confinement regime, and at some point it would cause the light-hole state with $j = \pm 1/2$ to become the hole ground state. The coupling with the electron state $1S_e$ yields a fourfold degenerate state, with angular momentum 0 (two states) and ± 1. The hole state with $j = \pm 3/2$ yields the second doubly degenerate state with momentum ± 1 and ± 2. In practice, the new lowest exciton level would be the state 0^L and the exciton fine structure resembles that of Fig. 2.3c.

Woggon and co-workers [10] calculated the electronic fine structure of a single CdSe nanorod, taking into account the typical electron–hole exchange interaction for their system (see Fig. 2.4). As expected, by varying the rod radius, two regimes could be identified: for a radius smaller than about 3.7 nm the arrangement of states reflects the well-known fine structure of a spherical nanocrystal, i.e. the lowest energy exciton has angular momentum ± 2. For larger radii on the other hand the exciton ground state has zero angular momentum projection along the major rod axis. This would induce a strongly polarized emission of light, as

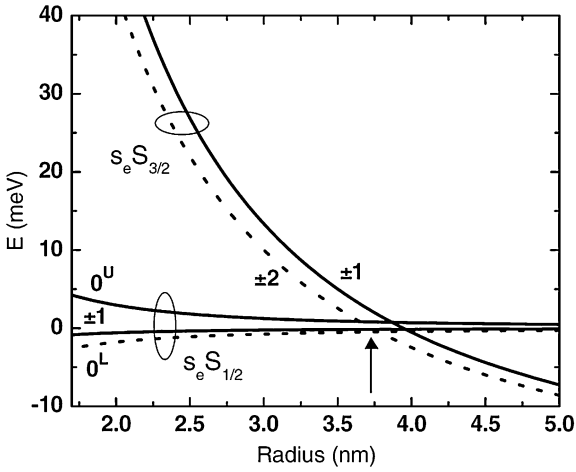

Fig. 2.4 Calculated exciton fine structure of CdSe nanorods. Taken with permission from Ref. [10]

opposed to the quasi-circularly polarized emission predicted for the ±1 excitons. Due to the small energetic separation among these states, thermal population processes give rise to novel phenomena in terms of polarization and carrier relaxation (as discussed later on).

2.5 Relaxation Mechanisms in Nanorods

The carrier mobility in nanorods has a 1D character [6], and this leads to optical properties in nanorods that are remarkably different from those of spherical nanocrystals, among them photoluminescence (PL) lineshape and polarization, radiative and nonradiative transitions, and their dependence on nanocrystal size and temperature. Their understanding represents a first step towards the exploitation of such nanostructures in optical devices. In this section we will discuss the basic optical properties of nanorods in terms of relaxation processes and spectral features, by stressing the differences between nanorods that are entirely made of one material (homo-structures) and those made by sections of different materials (heterostructures). We will distinguish the case of electron–hole relaxation inside the same material from that of relaxation concerning carriers localized in two different materials. In the first case, the possible optical transition is named of type-I, whereas in the second case is of type-II.

2.5.1 One-Dimensional Excitons in Homostructures

In the previous section we have described the fine structure of the ground state exciton in nanorods having a wurtzite structure. Here we will summarize the

experimental evidences collected by optical spectroscopy measurements, carried out on single nanorods and on ensembles of nanorods, and we will highlight the differences of nanocrystals with respect to the more traditional spherical nanocrystals. In nanorods, two confinement regimes can coexist, causing the transition energy to vary mainly as a function of the lateral confinement instead of the rod length. In Fig. 2.5 the effect is clearly visible from the absorption spectra of a series of CdSe nanorods of different diameters and lengths [14]. Two sets of five samples were analyzed in the study (Fig. 2.5). In one set (Fig. 2.5a), the nanorods had different lengths (12.5, 17.5, 25, 30 and 35 nm, from a to e) and comparable diameters (around 5 nm), while in the other set (Fig. 2.5a), the nanorods had different diameters (3.5, 4, 4.25, 4.5 and 5 nm from a to e) and comparable lengths (around 20 nm). By changing the nanorod length there was no appreciable shift of the optical transitions, whereas by increasing the radius an evident red-shift of the absorption peaks was observable.

Optical spectroscopy combined with scanning tunneling spectroscopy (STS) measurements, performed by Banin, Millo and co-workers [15, 16] and by El-Sayed and co-workers [14] have revealed a manifold of degenerate states which are split by crystal and shape anisotropy and by the electron-hole exchange interaction (see Fig. 2.6). These works anticipated the subsequent theoretical and experimental results on the exciton fine structure reported by Woggon and co-workers [10] (the reader can refer to chapter 3 for a more detailed discussion on the STS experiments).

Nanorod homostructures often show only one emission peak [17], corresponding to carrier relaxation from the lowest exciton state, similar to spherical nanocrystals. At room temperature, the PL broadening is around 70–100 meV for a sample of rods with narrow distributions of lengths and diameters. Such broadening [7], as in spherical quantum dots, is the result of two contributions,

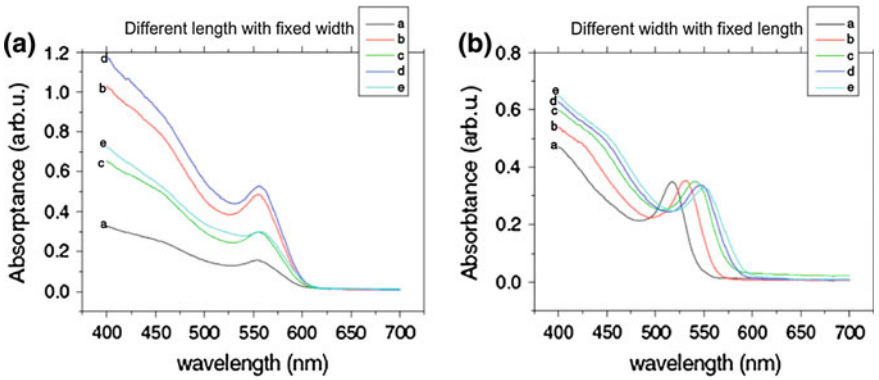

Fig. 2.5 **a** Optical absorption spectra of a series of CdSe nanorods with 5 nm width having different lengths of 12.5, 17.5, 25, 30, 35 nm. **b** Optical absorption of a series of CdSe nanorods with 20 nm length having different diameters of 2.5, 4, 4.25, 4.5, 5 nm. Reprinted with permission from Ref. [14]

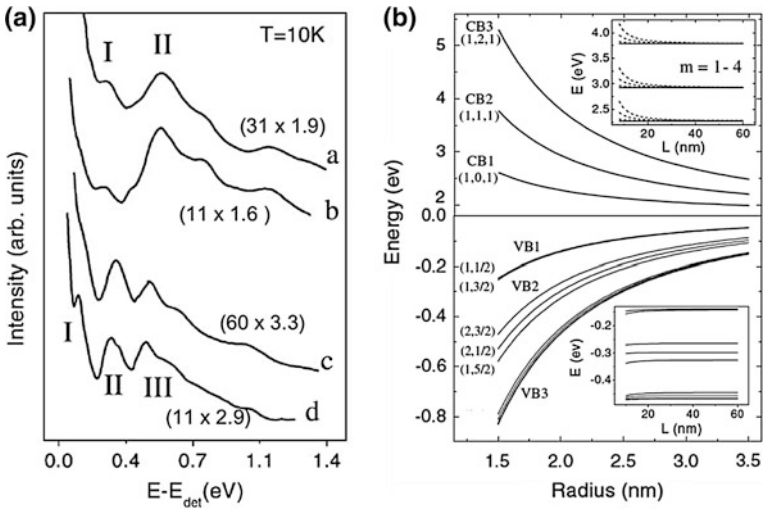

Fig. 2.6 **a** Photoluminescence excitation (PLE) spectra of CdSe nanorods of different sizes (corresponding length x diameter is indicated in brackets), showing peaks related to the first exciton transitions. It is evident that the diameter has a strong influence on the exciton level structure, whereas nanorods with different lengths but comparable diameter show similar spectra. The detection energy E_{det} was 2.25 eV for spectra *a* and *b*, and 2.03 eV for spectra *c* and *d*. **b** Conduction and valence band states distribution as function of the rod radius. Taken with permission from Ref. [15]

namely inhomogeneous and homogeneous broadening. Inhomogeneous broadening is mainly affected by the general quality of the sample and is related to the size dispersion, thickness fluctuations in single rods, quality of the rod surface, and it can be controlled (in principle) by improving these parameters. This type of broadening represents often an obstacle for the study of the intrinsic physical properties of semiconductor nanorods, and it can be bypassed only by performing experiments on single rods. Homogeneous broadening refers instead to coupling of charge carriers to phonons, is an intrinsic process and cannot be overcome by any improvement in synthesis. It will be discussed in detail in the following.

2.5.2 Temperature and Size-Dependence of the Exciton Relaxation Processes

After excitation, charge carriers inside a crystal tend to restore the initial state of equilibrium by losing their excess energy. As in all semiconductor systems, semiconductor nanorods undergo several possible relaxation pathways. In the present discussion, we separate such processes in two main categories, namely radiative processes (i.e. loss of energy by means of the emission of photons) and non-radiative processes (i.e. loss of energy via any other mechanism). The most

common non-radiative relaxation process is the creation of phonons (i.e. lattice vibrations) via carrier-phonon interaction, which leads to heating of the material. This coupling does not influence exclusively the decay of the carries towards lower energetic states, since in some particular cases it can promote the carriers into higher energy states, allowing them to escape from the material, by means of a process known as "thermal escape" [18–20]. Multi-carrier scattering processes are additional non-radiative relaxation processes, and they are all generally grouped in a class, the so-called "Auger-type" mechanisms [21–30]. They manifest when two or more electron-hole (e–h) pairs are present in the semiconductor, and consist in the transfer of the energy of an e–h pair to a third particle (electron, hole or exciton).

2.5.3 *Exciton–Phonon Interaction: Homogeneous Broadening*

The main features that distinguish nanostructures from bulk materials originate from the localized character of the electron and hole wavefunction and the discrete nature of their optical transitions. In the bulk, the broadening of the exciton line is mainly determined by the polar coupling of both electrons and holes to optical phonons [31]. The piezoelectric and deformation potential coupling of the carriers to acoustic phonons is usually not very important [32]. This situation is different in nanostructures, where the local charge neutrality character of the exciton becomes predominant, producing an ideal null polar coupling of the exciton to optical phonons [33]. This holds true for infinite barriers, for which the electron and hole wavefunctions are practically identical. In general, in real systems with a finite barrier a decrease of the polar coupling with increasing barrier is expected [33–35]. On the other hand, since the deformation potential coupling is proportional to $1/R^2$ (R being the radius of a spherical dot), the coupling strength to acoustic phonons is increased as the dimensions are reduced below the Bohr radius [32, 36]. Also the temperature affects each of these contributions. The temperature dependence of the spectral line width can be expressed as [37]:

$$\Gamma(T) = \Gamma_0 + \sigma T + \gamma N_{LO}(T) \tag{2.10}$$

where Γ_0 is the inhomogeneous broadening, σ is the exciton-acoustic phonons coupling coefficient, γ is the coefficient accounting for the exciton-optical (LO) phonon coupling and N_{LO} represents the Bose function for LO phonon occupation:

$$N_{LO} = \frac{1}{e^{E_{LO}/k_B T} - 1}. \tag{2.11}$$

In the expression above E_{LO} is the energy of the longitudinal optical phonon with momentum $k = 0$ (i.e. the phonon that preferably couples to the lowest exciton state) and k_B is the Boltzmann's constant. Due to the different energetic

dispersion curves of acoustic and optical phonons, the two couplings dominate at different temperature ranges. The acoustic phonons, having smaller energies (a few meV), contribute heavily to the broadening at low temperature (until 50–70 K [19]), whereas the optical phonons (with energies of a few tens of meV) dominate at higher temperature [19]. Nanorods having wurtzite structure, like CdS and CdSe, present a pronounced polar character, where the Frch interaction (with optical phonons) is the predominant coupling mechanism between charge carriers and optical phonons [38]. In the study of the exciton-LO phonon interaction, the fundamental quantity considered is the so called Huang-Rhys factor [34]. Experimentally, an estimation of the Huang-Rhys factor is possible by Raman spectroscopy, by simply considering the ratio of the signal intensity of the first to the zero order phonon replica [38]. Lange and co-workers [38] have performed Raman studies on CdSe nanorods and demonstrated an increase of the exciton-phonon coupling with decreasing rod radius, and the effect could be enhanced by growing a ZnS shell on the surface of nanocrystals acting as passivating layer (see Fig. 2.7). The Huang-Rhys factor remained below the bulk value, according to the model of Nomura et al. [34].

Quantum confinement affects not only the coupling strength of charge carriers with phonons, but also the energy of the LO phonons. This happens in quantum dots as well as in nanorods. Cardona and co-workers [39] have determined the dispersion of the LO phonons as function of the spherical nanocrystals size on the basis of the asymmetric lineshape of Raman spectra (Fig. 2.8). They found a decrease of the energy of the optical modes with decreasing size, and explained the low energy asymmetry of Raman spectra as due to the contribution of off-resonance vibronic modes.

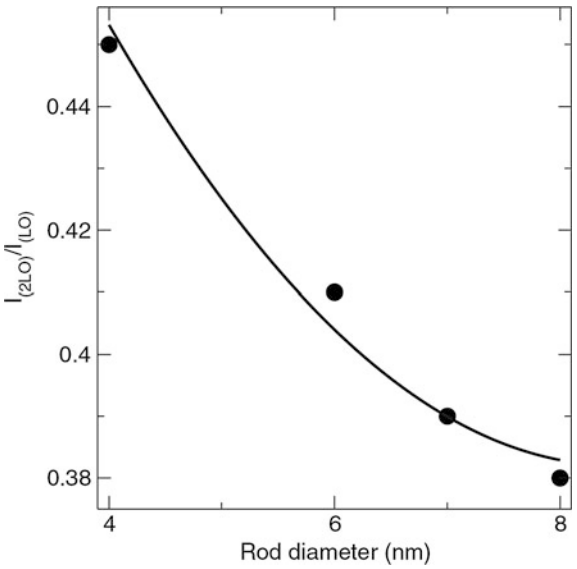

Fig. 2.7 Size dependence of the ratio between the second and the first order phonon replica of CdSe/ZnS nanorods. The solid line is a guide to the eye. Taken with permission from Ref. [38]

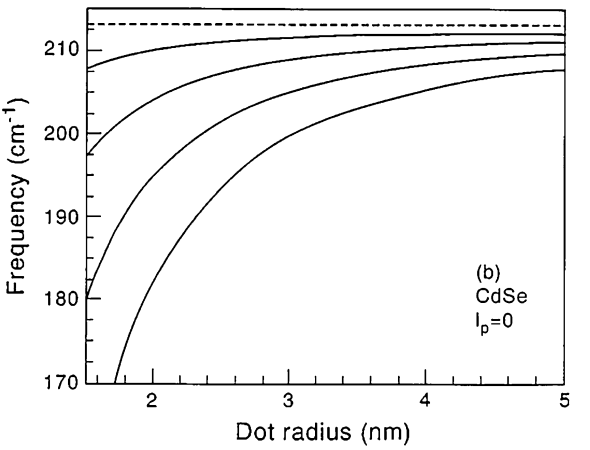

Fig. 2.8 Dependence of the first four optical-vibronic $l_p = 0$ modes on the CdSe dot radius. Taken with permission from Ref. [39]

In nanorods, the red-shift of the phonon modes becomes more pronounced, for example due to the loss of spherical symmetry which leads to the detection of vibrational modes with non-zero angular momentum. Lange et al. [38, 40] and Nobile et al. [41] have conducted independent studies (summarized in Fig. 2.9) on the role of quantum confinement on the optical phonon energies. They found a red-shift of the LO phonon energy with decreasing rod diameter, accompanied by a substantial independence on the aspect ratio. This red-shift can be understood in a simple picture by considering the negative dispersion of the optical phonon branches with respect to the transferred wave vector k, where $k = 2\pi/d$, d being the diameter of the nanorod. Detailed theoretical calculations of the confined phonon modes in high aspect ratio ellipsoids, supported by Raman experiments on CdSe nanorods, have resolved a fine structure of the phonon modes perpendicular and parallel to the long axis of the nanocrystals (Fig. 2.9). The energy of surface optical (SO) phonon modes can be approximated following the approach by Gupta et al. [42]:

$$\omega_{SO}^2 = \omega_{TO}^2 + \frac{\varpi_p^2}{\varepsilon + \varepsilon_m f(x)}; \;\; x = q \cdot d/2 \tag{2.12}$$

with:

$$\varpi_p^2 = \varepsilon_\infty (\omega_{LO}^2 - \omega_{TO}^2), \; q = 2\pi/L, \; f(x) = (I_0(x) \cdot K_1(x))/(I_1(x) \cdot K_0(x)) \tag{2.13}$$

where I and K are Bessel functions. Therefore the SO phonon energy depends on both the length L and the diameter d of the nanorods [41–43].

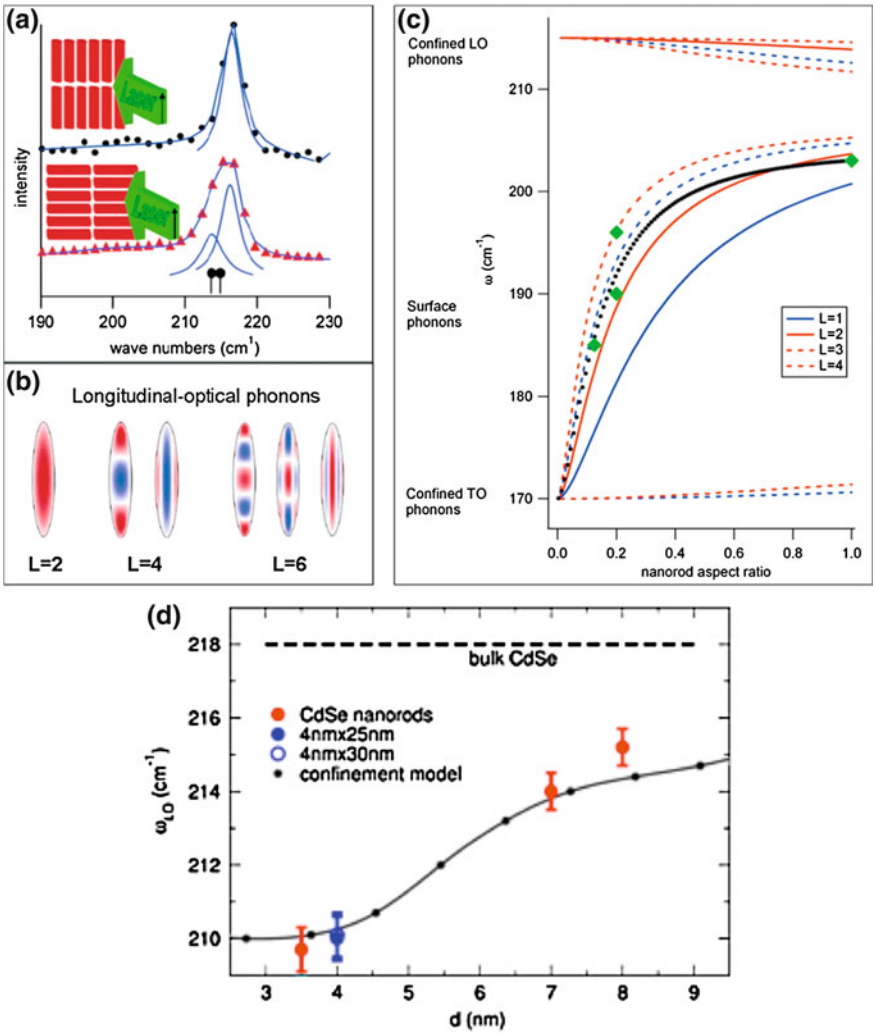

Fig. 2.9 **a** Raman spectra showing the LO phonon mode excited with light polarized parallel and perpendicularly with respect to the long axis of the nanorods. **b** Cross sections of the calculated phonon potential for the LO Raman-active odes with $M = 0$ and different angular momentum L. (a) and (b) are taken for Ref. [119] **c** Calculated energy of the different phonon modes versus the rod aspect ratio. The red and blue lines are calculated from the model in Ref. [119], the black line shows the dispersion of the SO modes according to the model of Gupta et al., and the green dot are data points from Ref. [120]. **d** Frequency of the LO-phonons as a function of rod diameter Taken with permission from Ref. [40]

2.5.4 Auger Effects in Nanorods

Multicarrier Auger effects play a fundamental role in the relaxation processes of nanostructures. Auger recombination represents a limitation for the use of nanostructures in optical devices requiring optical gain, since non-radiative multiparticle scattering hinders the desired population inversion. However, the Auger efficiency can be significantly reduced by a wise choice of materials and via engineering of the band alignment and wavefunction localization [44–46]. The physical interest on the Auger processes resides in the role played by the quantum confinement on the assignment of the new selection rules and the Auger efficiency in nanoparticles with respect to the bulk. Quantum confinement increases the Coulomb interaction between the charge carriers inside the nanomaterial with respect to the bulk counterpart. Moreover, the translation momentum conservation acting in bulk materials is broken in nanoparticles, allowing for more efficient Auger processes [21, 47, 48]. On the other hand, the discreteness of electronic states in nanocrystals should imply a reduced availability of states that can satisfy the energy conservation condition, whereas in the bulk a continuum of states is always guaranteed (in this sense, Auger recombination would be more efficient in the bulk). The interplay of both contributions determines the net effect in each system. In this regard, several differences arise when considering nanorods instead of spherical nanoparticles.

Since the Auger recombination rate is strongly sensitive to the carrier density and consists in e–h pair annihilation, such a mechanism affects the temporal trend of the relaxation processes. Therefore, the general procedure for studying Auger mechanisms occurring in nanoparticles consists in time resolved (TR) measurements of both the PL (TRPL) and the transient absorption (TA) as function of the photogenerated carrier density. The simplest way to analytically describe an Auger process is to consider the following equation [30]:

$$\frac{dn}{dt} = -C_A(M)n^M \tag{2.14}$$

This equation expresses the decay rate of the average population density n in the presence of M interacting particles (intended as electrons, holes or excitons). The key parameter is the Auger constant $C_A(M)$ which corresponds to the actual probability for the Auger process to occur. It is dependent on the average number of interacting carriers in the system considered. The general solution of Eq. (2.14) is:

$$n(t) = \frac{n(0)}{\left(1 + \frac{1}{M-1} C_A(M) n(0)^{M-1} t\right)^{M-1}} \tag{2.15}$$

This expression is employed to extract the Auger constant by means of a fitting procedure of $n(t)$, which is given by the measured temporal decay; the quantity $n(0)$ is usually known, while M is often kept as parameter. M becomes a key

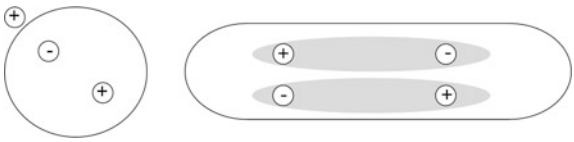

Fig. 2.10 Sketch of the exciton extension in spherical (*left image*) and rod-shaped (*right image*) nanocrystals and relative implications in Auger processes. In spherical nanocrystals the interacting charge carriers can be considered independent, giving M = 3, whereas in nanorods four carriers (two e–h pairs) can be considered as two interacting particles (two excitons), giving M = 2

parameter if one wants to determine in which regime Auger mechanisms take place. In quantum confined systems, there are two main types of mechanisms: three-carrier relaxation and biexcitonic Auger relaxation. The first occurs in the strong 0D confinement regime and provides $M = 3$, whereas the second gives $M = 2$ and occurs in the case of a 1D system. In strongly confined 0D nanocrystals the Coulomb contribution to the exciton energy is negligible with respect to the confinement term (see discussion at the beginning of this section). This makes it possible to consider the charge carriers in the dot as independent particles, thus producing a cubic behavior in Eq. (2.14) [21]. The minimum number of carriers allowing Auger relaxation is then $M = 3$, i.e. the energy possessed by an e–h pair is transferred to a third carrier. In the case of nanorods, e–h pairs give rise to 1D excitons, since the exciton extends along the long axis of the nanorods (see Fig. 2.10). Along that direction, the confinement energy can have a smaller contribution with respect to the Coulomb interaction, allowing for the formation of a 1D exciton. Therefore, in terms of Auger mechanism, one must consider two excitons as the minimum number of interacting particles, thus $M = 2$, as one exciton can transfer its energy only to a second exciton.

Comparative studies carried out on spherical nanocrystals and on nanorods with various aspect ratios have provided an estimate of the size ranges of the two regimes and of the relevant Auger constants. Klimov and co-workers have demonstrated that below an aspect ratio AR = 8 charge carriers in nanorods behave as uncorrelated particles, whereas above this value e-h pairs organize themselves in 1D excitons and recombine via a biexcitonic Auger process [29]. The Auger constant that gives a measure of the Auger efficiency in systems with the same volume was found to be larger in nanorods than in spherical nanocrystals of equal volume. In Fig. 2.11 we show this result in terms of Auger lifetime (which is inversely proportional to the Auger constant), as derived from Ref. [29]. This behavior has been ascribed to the major surface contribution to the matrix element of the Auger transition: nanorods have a larger surface area when compared to spherical nanocrystals of equal volume, and this should lead to a larger Auger constant [29].

The surface plays also a non-trivial role in defining the optical properties of nanorods, especially for what concerns the existence of surface states and their influence on the carrier dynamics. The efficiency of the Auger processes may be

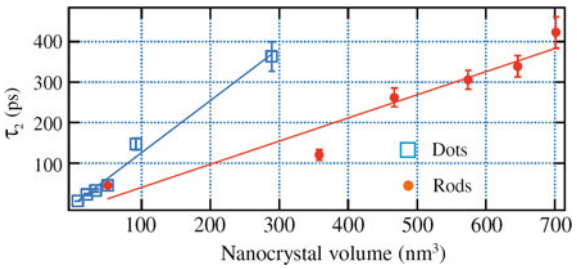

Fig. 2.11 Auger time constant of two e–h pairs recombining in dots (*blue symbols*) and rods (*red symbols*), as a function of the nanocrystal volume. Taken with permission from Ref. [29]

affected by means of trapping at such states [48]. This has important implications on the carrier cooling from higher excited states to the band-edge, which depends on the Auger efficiency, as demonstrated by Klimov and co-workers [28]. In their study, they showed that in nanorods multicarrier generation can cause an Auger heating, consisting in the increase of the energy of an exciton, as a consequence of an energy transfer event deriving from a second exciton recombination. The consequent increase in carrier temperature competes with the more classic phonon emission as a relaxation channel, and decreases the carrier cooling in the high excitation density regime.

2.6 Single Nanorod Properties

As said before, CdSe represents perhaps the most studied system among the spherical and elongated semiconductor nanoparticles. They are commonly considered as prototype materials in the study of the optical properties of single nanoparticles with wurtzite structure. Lorentzian lineshape, spectral diffusion, and intermittent emission (called "blinking") are some of the properties shared by single spherical and elongated nanocrystals [11, 49, 50]. Defect states can induce charge accumulation by classical carrier trapping at defects lying at energies lower than the band gap, which occurs following an excitation. Irregularities in the nanocrystal shape can lead to charge storage in absence of an excitation, if a distribution of a permanent surface charge can be created. This happens when the rod does not extend perfectly along the wurtzite c-axis, but is twisted with respect to such axis, which can be realized if some stacks of unit cells along the c axis do not span the whole length of the rods, thus creating tiny polar facets along the lateral sides of the rod (see Fig. 2.12). In such a situation, as observed by Krishnan et al. [50], a net surface-charge density is found at the surface of the rod.

The exposed cells are characterized by uncompensated charges, giving rise to an accumulation of a density of charge. The propensity of charges to distribute easily on the rod surface influences strongly the optical properties of single nanorods, especially for what concerns the emission energy and its intensity. For single nanorod experiments, major efforts have been made towards the comprehension of both the role of the surface on the localization and recombination of

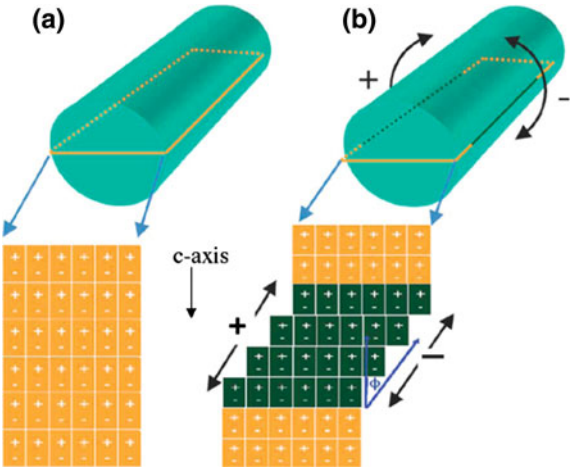

Fig. 2.12 Representation of two different rods grown along a parallel **a** and a tilted **b** direction with respect to the c-axis of the wurtzite structure. In the first case, the rod is a perfect cylinder, and no polar facets are created at the lateral sides of the rod. In the second case, the rod has a more irregular shape, which can lead to exposure of tiny polar facets at the lateral sides of the rod

carriers, and on its impact on the polarization of emission and on the exciton fine structure.

Single nanorod spectra present more complicated dynamics in the temporal evolution of the emission energy, line shape, and intensity, when compared to spherical nanocrystals. Under continuous wave excitation, nanorods show the typical intermittent behavior, as observed in other well-studied systems. At low temperature, single rod spectra are characterized by a broadening of the order of a few meV, and have in general an asymmetric line shape [10, 11, 51]. This asymmetry, which is observable only at temperatures below 15 K, can be ascribed to several reasons. These include charged excitons, fine structure of the lowest excitonic state, acoustic phonon contributions and influence of internal electric fields. In the following, we will discuss the single contributions of phonons, charged excitons, as well as internal and external electric fields, on the spectral features of single rods.

2.6.1 Charged/Neutral Excitons and Phonon Contributions

The role of charged excitons on the spectral features has been studied extensively by means of PL measurements at low temperature, which were performed as a function of the excitation density [11]. The fundamental difference between charged and neutral exciton spectra lies on the effect of the excess of charge on the fine structure of the lowest excitonic state. For neutral excitons a double peak emission usually arises from single nanorods at low temperature ($\sim$5 K), and is assigned to intrinsic bright states. This feature vanishes at higher temperature, as thermal population contributes to a state mixing. The spectral line shape of Fig. 2.13, can be explained by the theoretical fine structure, as discussed by Woggon et al. in Ref. [10]. As shown in Sect. 2.4 (Fig. 2.4) nanorods experience

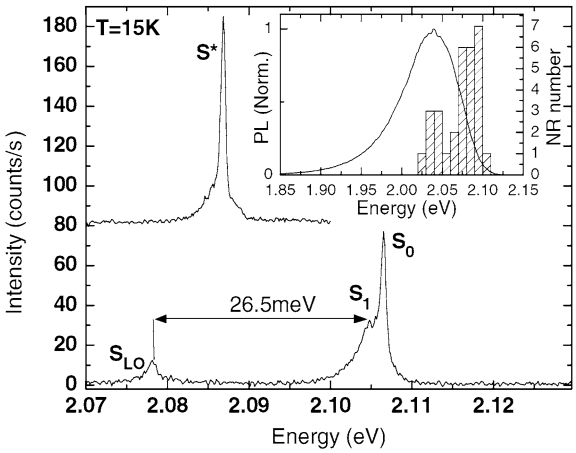

Fig. 2.13 Two single CdSe rod spectra detected at 15 K. The upper part corresponds to a charged exciton spectrum, showing fine structure due to excess charge, whereas the bottom spectrum refers to a neutral exciton, showing peaks (labeled as S_0 and S_1) belonging to the rod fine structure. Inset: statistics on 30 single nanorods. Taken with permission from Ref. [10]

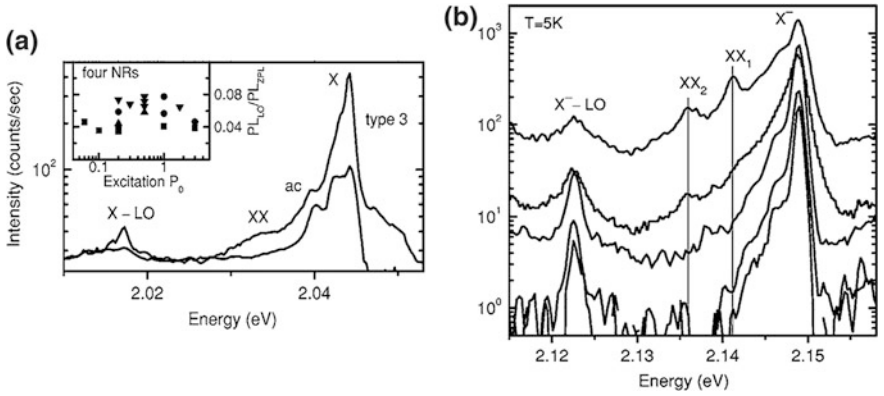

Fig. 2.14 Power dependence of a single rod emission for a neutral exciton **a** and a charged exciton **b**. Taken with permission from Ref. [11]

an inversion of the ground state fine structure below a critical rod radius of $\sim$3.7 nm, which induces a change in the effective ground state of the rod.

Nanocrystals with spherical symmetry have a fixed dark ground state that is characterized by a momentum projection of ± 2. Nanorods with radius smaller than 3.7 nm have instead a ground state with projection 0 (dark, labeled 0^L, contrary to the higher energy, bright 0^U state). Despite the dark nature of the state 0^L, its proximity to the nearest bright state (labeled ± 1) is of the order of some μeV, which allows the thermal population of the bright one at very low temperature. In this sense, it is common to assign the dual nature of the single rod spectra (the

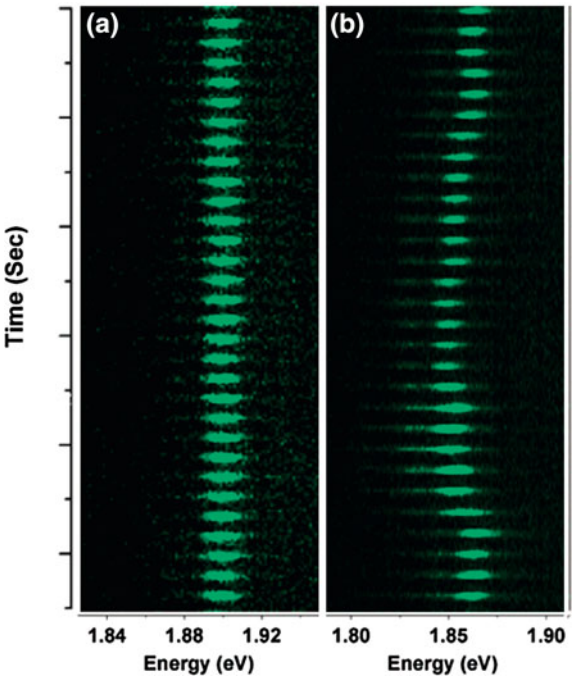

Fig. 2.15 Temporal evolution of the PL spectra of two representative CdSe nanorods. The rod in (**a**) shows very stable emission, while the emission features of the rod in (**b**) are fluctuating due to local electric fields induced by unstable charge localization along the rod. Taken with permission from Ref. [52]

peaks S1 and S0 of Fig. 2.13) to the emission of the lowest bright states ± 1 and 0^U. PL spectra showing the fine structured exciton ground state are considered a fingerprint of neutral exciton emission. For a charged exciton (trion) the fine structure is expected to vanish due to the excess charge present in the rod [11]. The charged exciton peak is shifted with respect to the neutral exciton due to Coulomb interaction in the trion system. In addition, at high excitation density also the recombination from biexcitons (XX) can be observed (see Fig. 2.14).

2.6.2 *Influence of Electric Fields on the Optical Properties of Single Nanorods*

Stark effect experiments, i.e. the study of the impact of an external electric field on the electronic structure, represent the most common approach to study and control the carrier localization along the rod. Fluctuations in the emission energy, PL intensity and broadening are the main distinguishing quantities in nanorods [52]. Figure 2.15 shows typical time traces from two different nanorods belonging to the same sample of CdSe nanorods, measured at 10 K, under CW excitation and without external electric field [52].

At first glance, the two rods have dissimilar emission energies, broadening and relative temporal evolutions. In particular, rod A shows a very stable behavior,

consisting of an unmodified PL spectrum over time, whereas rod B shows considerable instability, as if it underwent mutating conditions during its emission process. Systematic studies carried out on large sets of nanorods [53] and by continuous monitoring of the same nanorod, have indicated a close correlation between the emission energy, the broadening and the intensity of the PL signal. As a general trend, a red-shift of the emission energy corresponds to an increase of the full width at half maximum (FWHM) and a decrease of the emission intensity (Fig. 2.16) [52].

Interestingly, such a behavior can also be induced by applying an external electric field, as shown in Fig. 2.17. Here, a bimodal switching effect is seen when an electric field is applied to the nanorods, which either turns the PL of some rods off or turns the PL of some others on. This behavior can be understood considering the effect of the surface and the elongated shape of the rods, which can

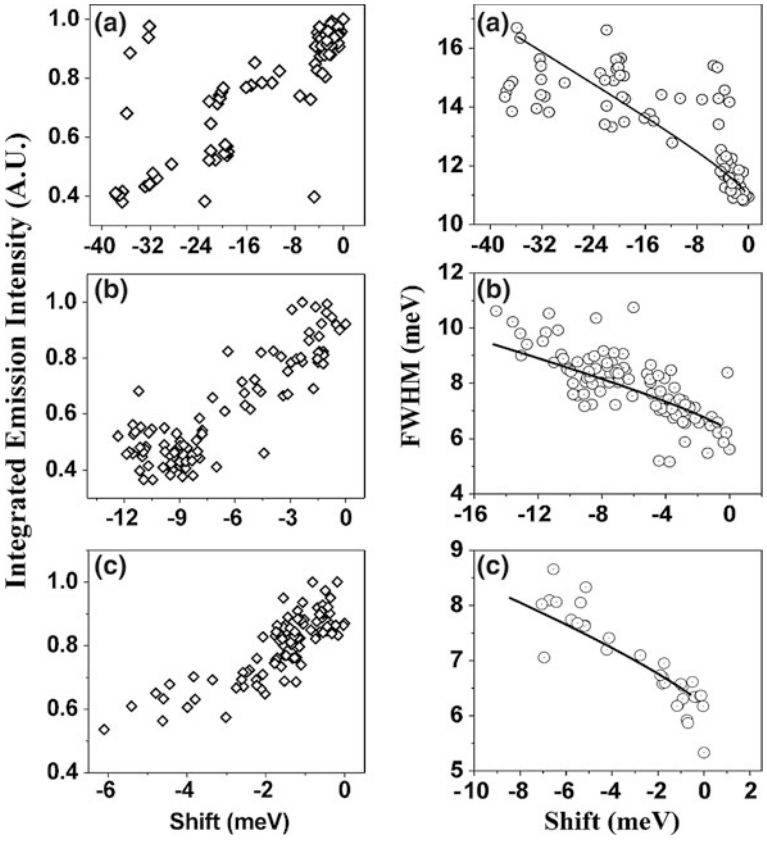

Fig. 2.16 Statistical analysis of the emission properties of three single nanorods subject only to local field effects. *Left panels* show the integrated PL intensity reduction with increasing red shift. *Right panels* correlate the spectral broadening to the energetic shift: a red shift corresponds to an increased FWHM. Taken with permission from Ref. [52]

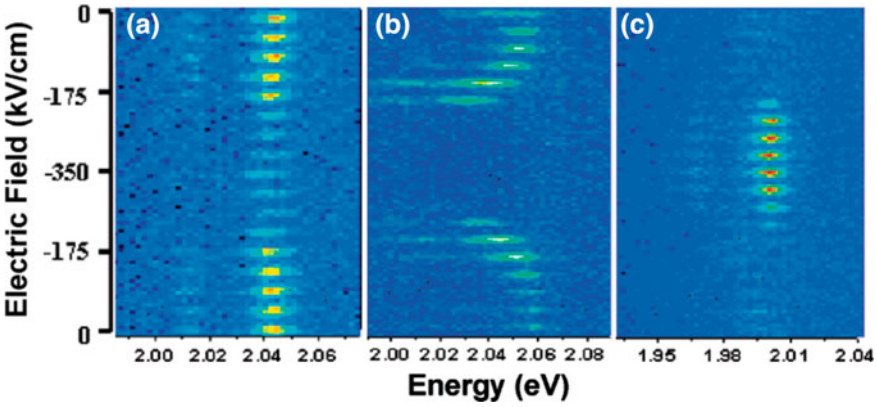

Fig. 2.17 Switching single nanorods due to external electric fields. The three panels show the emission behavior of three rods located in between interdigitated electrodes under applied bias. The emission of the rods in **a**, **b** is switched off due to electric field, where rod **b** also exhibits **a** red shift, while rod **c** is switched on. Taken with permission from Ref. [52]

lead to a varying overlap of the electron–hole wave functions. Such variations can have either extrinsic or intrinsic sources. Extrinsic sources are for example external electric fields, whereas intrinsic sources could be related to the dynamics of carriers from/to surface trap states, which induce the formation of varying local fields. If on one hand the elongated shape offers the possibility to localize the e–h wave functions in several configurations, the extended surface of the nanorods contributes heavily to the creation of numerous trap sites, at which carriers can be localized.

When nanocrystals are subject to an external electric field, they experience the so-called quantum confined Stark effect (QCSE), which induces a red shift of the optical transitions (both in absorption and emission), a decrease of the transition probabilities [52] and an increase of the spectral broadening. As an example, Fig. 2.18 provides a qualitative description of the exciton distortion induced by the application of an electric field. For nanorods aligned along the electric field direction, electrons and holes are pulled in opposite directions, towards the ends of the rods. The result is that their wave function overlap is reduced, and the optical transition red-shifts and decreases in intensity (due to a decrease in the oscillator strength). The process depends strongly on the mutual orientations of the electric field and the long axis of the rod: if they are parallel, the effect is maximized, whereas if they are perpendicular the influence of the electric field is negligible (Fig 2.18).

Concerning the correlation of the broadening of the emission peak with the PL intensity and the emission energy we refer to the treatment of Ref. [52]. The starting point is to consider the energetic shift caused by an electric field up to the second order:

$$\Delta E = \mu\varepsilon + \frac{1}{2}\alpha\varepsilon^2 \tag{2.16}$$

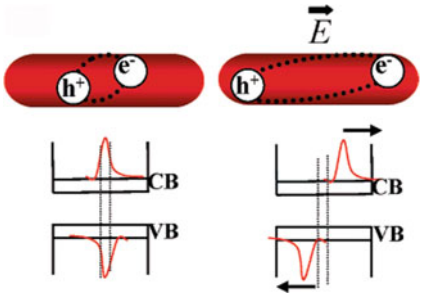

Fig. 2.18 Effects of local electric field on the exciton extension along the rod, leading to a reduction of e–h overlap. Taken with permission from Ref. [52]

Here, ΔE is the energy shift, ε is the electric field (due to external or local fields), μ the dipole moment and α the polarizability. By differentiating Eq. (2.16) one can obtain the expression for the predicted change in the spectral width:

$$\delta(\Delta E) = (\mu + \alpha\varepsilon)\delta\varepsilon \tag{2.17}$$

μ and α can be found experimentally by Stark effect measurements. $\delta\varepsilon$, if referred to fluctuations of local charges, is related to the distance of such charges from the exciton and then to the spatial fluctuation [52].

2.6.3 Polarization Properties

The polarization properties of nanorods represent one of their distinctive characteristics with respect to other colloidal nanocrystals, like for example spherical quantum dots, and have received much attention recently (both from the theoretical and experimental point of view). As previously discussed, the electronic structure of rods is strongly affected by their size and shape, in particular by their aspect ratio (AR). The fine structure of the lowest exciton state is the dominating factor in defining not only the character of the emitting state (whether dark or bright) but also the polarization properties. Since we deal with nanostructures with AR > 1, only the component of the angular momentum having projections along the z long axis of the rod should be considered. In particular, in nanorods a symmetry change of the 1D exciton ground state occurs at a certain radius [10] or AR [54], as was already discussed in Sect. 2.4.

Here, the optical transition should be strongly polarized along the wurtzite c-axis (axis z in Fig. 2.19), with an increasing polarization degree with increasing AR. Polarization spectroscopy on single nanorods provides experimental proof of the theoretical predictions. Polarized emission up to 80 % has been demonstrated for CdSe nanorods with AR > 2 [17] whereas for spherical nanocrystals only values up to 10 % were obtained, see Fig. 2.20b.

Excitation polarization measurements demonstrated the optical transition polarization of nanorods both in one- [55] and two- [56] photon-excitation experiments, as displayed in Fig. 2.21. In the one-photon experiment, the

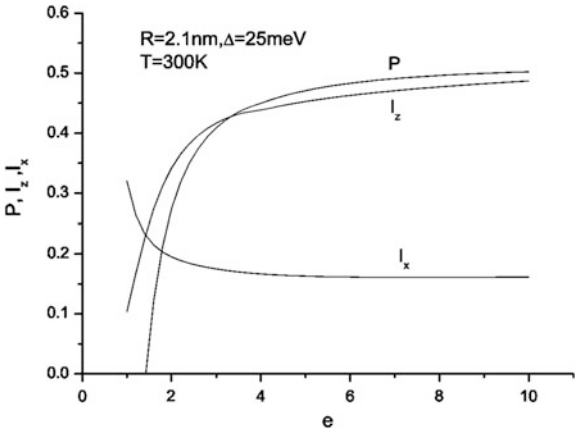

Fig. 2.19 Example of theoretical polarization variation of rods having a fixed radius and varying aspect ratio (*e*). Taken with permission from Ref. [54]

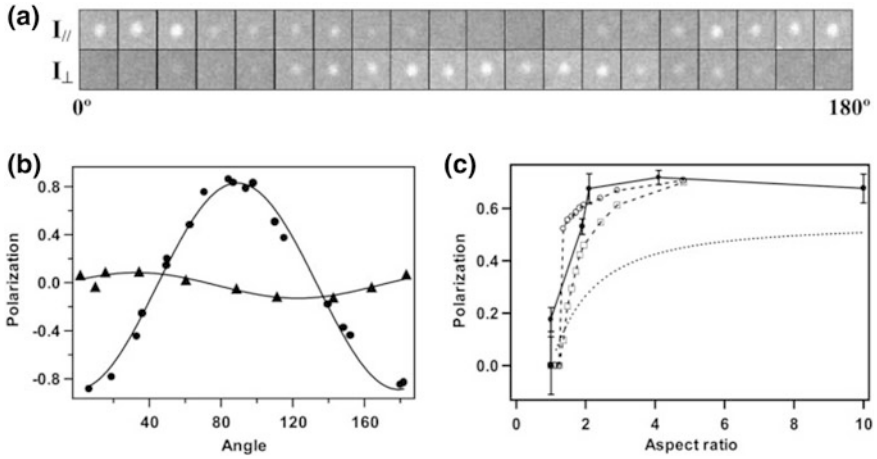

Fig. 2.20 **a** Imaging of the emission of a single rod recorded in mutually perpendicular polarization directions simultaneously. **b** Plot of the polarization degree as a function of the rotation angle of the nanorods in **a** (*solid circles*) and the polarization for a single spherical nanocrystal (*triangles*). **c** Experimental polarization factor as a function of the aspect ratio of the rods. Taken with permission from Ref. [17]

polarization curve followed the typical $\cos^2(\Theta)$ function, whereas a dependence on $\cos^4(\Theta)$ was found in two-photon excitation, according to the nonlinear character of the two-photon absorption process. The level crossover occurring in nanorods and proposed by diverse theoretical approaches [10, 17] allows to understand the polarization dependence of the nanorods excitation. Indeed, the ground state becomes bright in rods, allowing for the absorption of polarized light along the major *c*-axis.

Experimental [57] and theoretical [58] studies on free standing InP nanowires showed that the polarization properties of the band edge transition in one-dimensional semiconductor nanostructures depend both on the intrinsic level structure, which shows p-type wave function characteristics, and on the geometry of the dielectric environment of a cylindrical structure where the diameter is much smaller than the wavelength of the light (Fig. 2.21c–d). In this case, the light wave component along the wire is not reduced, while the component perpendicular to the wire is strongly attenuated. The combination of these two effects can explain the giant polarization of the band edge transition, of up to 96 %, that was observed in InP nanowires. Temperature dependent polarization measurements can help to distinguish between the band structure and the geometrical contributions, as the first should depend on the temperature, while the second should not.

2.7 Nanorod Heterostructures

We will now discuss different types of nanorod heterostructures and their respective optical properties, as well as their potential for device applications. Our main focus will be on semiconductor heterostructures consisting of materials with different band gaps, and we will briefly mention also semiconductor–metal heterostructures. Many excellent reviews have appeared recently on this topic [59–62], and the reader is directed to those reviews for more in-depth coverage. Figure 2.22a shows some of the nanorod heterostructures that have been reported so far by various groups, while Fig. 2.22b shows two possibilities of band alignment for semiconductor heterostructures, namely type-I and type-II. In type-I heterostructures, the optically excited carriers are confined in the lower band gap material, whereas in type-II heterostructures the electrons are localized in one material, and the holes in the other material. As we will see shortly, for some materials the band alignment can be tuned from a type-I to quasi type-II, where the holes are localized in one material and the electrons are delocalized over the whole nanostructure, via quantum confinement effects. In many cases, the appropriate choice of materials and the geometry allows to obtain suitable energy gaps for the targeted application. Among the rod-like heterostructures that have been fabricated so far, we find dot-in-a-rod structures [53, 63, 64], collinear nanorods [65–71], nanobarbells [72, 73] and magnetic-semiconductor nanorods [74, 75].

2.7.1 Semiconductor Dot/Rod Heterostructures

This particular type of nanorod heterostructure is characterized by a spherical core of material A and a rod-shaped shell of material B, as illustrated in Fig. 2.23 for two different material combinations that result in type-I and type-II band alignment, respectively. In the type-I structure, electrons and holes are localized in the

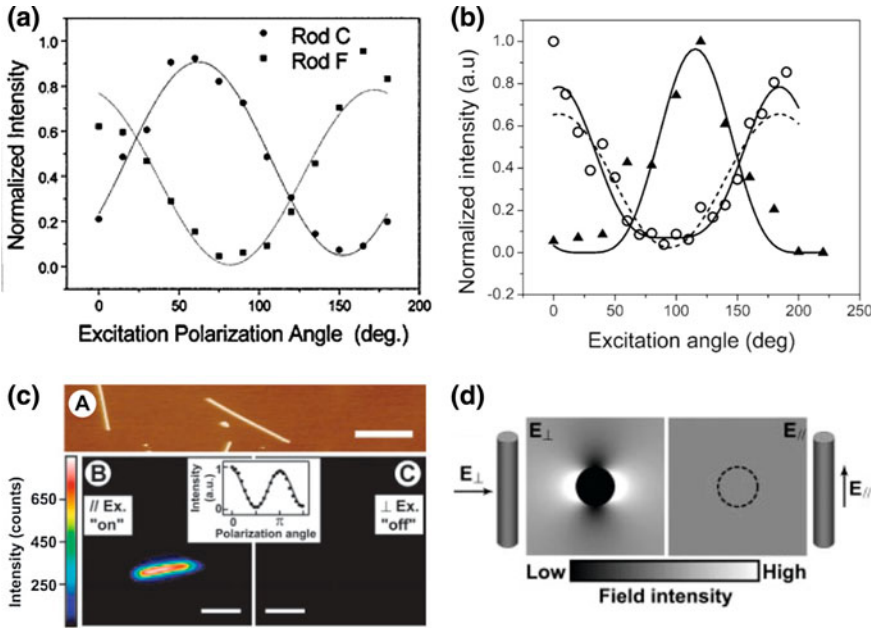

Fig.2.21 **a** Polarized excitation measurements performed on two single nanorods (*symbols*) and relative best fit curves (*continuous lines*) to the $\cos^2(\Theta)$ function of the excitation angle. Taken with permission from Ref. [55]. **b** Polarized excitation experiment carried out by two-photon excitation. Symbols represent the experimental data, whereas continuous lines are the best fit curves to the $\cos^4(\Theta)$ function. Taken with permission from Ref. [56]. **c** AFM image of InP nanowires (scale bar = 5 micrometer) (*A*), and the PL emission intensity of a single InP nanowire recorded with exciting light polarization parallel (*B*) and perpendicular (*C*) to the nanowire. The scale is 3 micrometer. **d** Dielectric constant model for light polarization parallel and perpendicular to a cylinder. **c** and **d** are taken with permission from Ref. [57]

same spatial region, namely the core region, before recombination, because both the lowest electron state and the highest hole state reside in the same material. In several reported cases, however, the electrons are delocalized over the whole rod volume due to the small conduction band offset [53, 76, 77]. The situation is different for type-II structures, where the minimum of the conduction band and the maximum of valence band are located in different materials regions of the system. This makes a type-II transition from the minimum of the conduction band in material A (rod-shell) to the maximum of the valence band in material B (core) possible.

In the following, we will focus on the case of the CdSe/CdS dot/rod system sketched in Fig. 2.23 (left panel), where a spherical CdSe core is embedded in an outer CdS rod. Typical absorption and emission spectra of such nanorods are displayed in Fig. 2.24 [78, 79]. We find that the absorption is dominated by the CdS shell, whereas the emission originates from states related to the CdSe core. This behavior is clearly advantageous for the optical emission properties, because a large 1D system (i.e. the entire rod) is capable is harvesting the excitation light, whereas

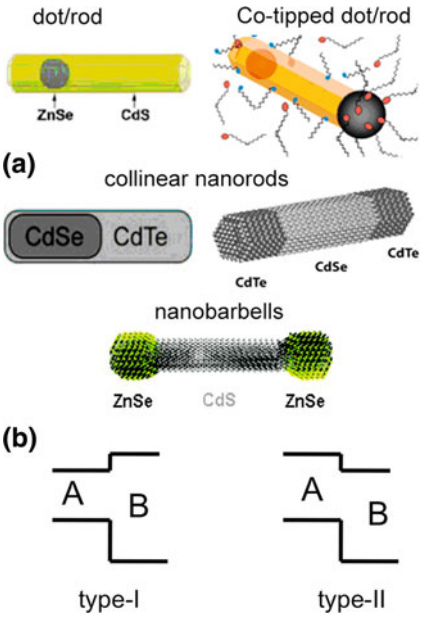

Fig. 2.22 **a** Examples of heterostructured nanorods: dot/rod, Co-tipped, collinear nanorods and nanobarbells. **b** Band alignment of type-I and type-II heterostructures

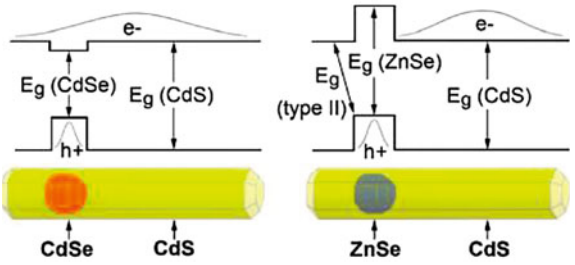

Fig. 2.23 Sketches of two possible nanorod heterostructures that have been synthesized by wet-chemical approaches, and relative band-alignment and e–h wavefunction localization Taken with permission from Ref. [63]

the emission comes from a small 0D system with well-defined level structure, i.e. the CdSe core.

In order to better interpret the experimental data, theoretical absorption spectra were calculated using the envelope function approximation [64], which allowed to assign the strong onset in absorption at higher energy to the lowest excitonic transition of CdS, while the much smaller peak at lower energy could be assigned to the transition occurring in the CdSe core. The emission peak was slightly red-shifted with respect to the lowest CdSe absorption, suggesting a direct origin from the core. The photoluminescence excitation (PLE) measurements on two representative samples of nanorods having different ARs 6 and 19, respectively, (see Fig. 2.25) confirmed this result [64]. The narrow line width of the peaks in PLE at low temperature made it possible to resolve the phonon replica of the PL emission. Here, the energy shift of the phonon replica was 26 meV, which corresponds to the LO phonon energy in CdSe and therefore provided a clear proof that the emission originated from the core material (Fig. 2.25).

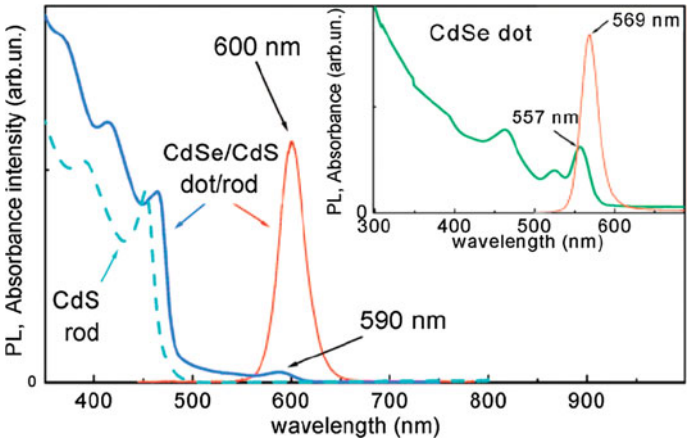

Fig. 2.24 Absorption (*blue*) and photoluminescence (*red*) of core–shell nanorods. The absorption is dominated by the nanorod shell due to its much larger volume with respect to the core. The emission peak is slightly red-shifted with respect to the first absorption peak related to transitions of the core. The *dashed line* shows the absorption of CdS only nanorods, and the inset displays the absorption and emission of spherical CdSe nanocrystals that were used as seeds for the core–shell rod synthesis. Taken with permission from Ref. [78]

2.7.2 Electron–Hole Dynamics in Core–Shell Nanorods

Pump-probe transient absorption measurements have been performed to study the carrier dynamics in core–shell nanorods [80]. In such experiments the sample is excited by a short pulse at a specific wavelength, and then the relative change in transmission $\Delta T/T$ is measured at defined delay intervals (normalized by the transmission without prior excitation). The normalized relative transmission reflects the population of the electronic levels caused by the excitation pulse. Such pump-probe experiments have revealed the role of surface and interface states in core–shell nanorods [80]. As an example, a recent work studied the ultrafast electron–hole dynamics of CdSe (spherical core)/CdS (rod shell) nanocrystals and pointed at electron delocalization even for the low energy transitions in these systems [78]. Figure 2.26 shows $\Delta T/T$ spectra at different time delays for two excitation energies: high energy at 390 nm exciting carrier in the CdS shell, and low energy at 590 nm exciting carriers in the CdSe core. At high excitation energy, a strong instantaneous photobleaching for the levels associated with the shell is observed (at around 460 nm), followed by a much slower build up of a peak at 590 nm due to carrier relaxation into the core. However, in the case of excitation of carriers in the core levels, also an instantaneous photo-bleaching at 460 nm is observed. This indicates bleaching of the electronic states of the shell, due to the delocalization of the electrons in the conduction band. As we will see later on, many optical experiments can be explained assuming electron delocalization in such nanostructures.

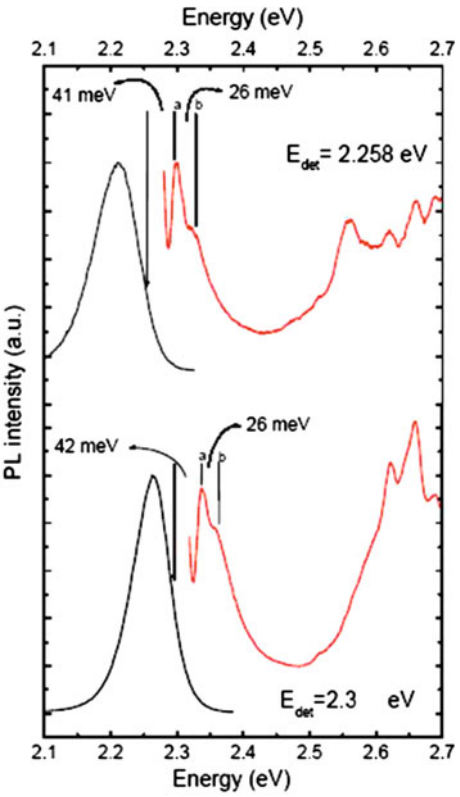

Fig. 2.25 PL (*black lines*) and PLE (*red lines*) spectra of two representative samples of CdSe/CdS nanorods having aspect ratios equal to 19 (*top*) and 9 (*bottom*), as recorded at 10 K. The detection energies are indicated by the *arrows* on the *blue* side of the PL. The lowest resonances in the PLE signal correspond to the ground state resonance **a** and its phonon replica **b**. Reprinted with permission from Ref. [64]

2.7.3 Photoluminescence Studies on Single Core–Shell Nanorods

Mueller et al. studied the optical properties of single nanorods developed by the classical wet-synthesis method and determined the role of surface charges on the spectral position, intensity and broadening [76]. Figure 2.27a shows two PL spectra recorded from the same core–shell nanorod at different times, manifesting fluctuations of the PL peak over time. They could correlate this spectral jitter to fluctuations of the charges on the surface of the nanorods [76]. In nanorods, in contrast to spherically symmetric nanostructures, these fluctuations can strongly influence the electronic level structure via the quantum confined Stark effect (QCSE). In detail, when the surface charges are close to the core, where the

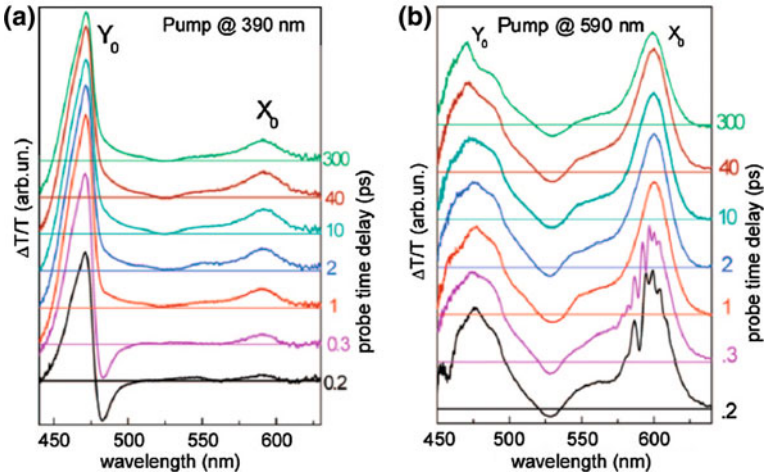

Fig. 2.26 Normalized transient absorption spectra recorded from core-shell nanorods fabricated by the seeded growth method. **a** Excitation energy corresponding to transitions in the CdS shell, **b** and corresponding to transitions in the CdSe core. Taken with permission from Ref. [78]

emission occurs, the PL peak is red-shifted and broadened due to the Stark effect, and when the surface charges are localized at the far end with respect to the core, the PL occurs at higher energy and with a sharper line width (Fig. 2.27b, c).

These findings point directly to the possibility to tailor the wave function distribution by the aspect ratio of the nanorods, which was further discussed by Mueller et al. [53]. In addition to the aspect ratio, Muller et al. demonstrated that also external electric fields can be used to tune the nanorod emission intensity and wavelength [53, 81]. Also the Fer energy transfer between nanorods and organic dye molecules (Fig. 2.27d, e) could be tuned by external electric fields in a way that the emission originated from the nanorod at zero electric field, and from the organic dye when an electric field was applied. Controlled switching in between these two states is shown in Fig. 2.27f, g, h. In these core–shell nanorods, the wavefunction distributions of the electrons and holes could be modified strongly by an external electric field, from a configuration with large overlap of electrons and holes in the core region, to a spatial separation where the holes were localized in the core and the electrons forced to the opposite tip by the electric field. In the latter case, the emission intensity was largely reduced due to the small spatial overlap of the electron and hole wave functions, and the emission was red-shifted due to the band bending, as shown in Fig. 2.28a. Indeed, Kraus et al. [81] showed that exciton emission could be quenched by the electric field and that it could be recovered after microsecond time scales by switching the electric field off, as shown in Fig. 2.28c, e.

The screening of the Stark effect by high intensity excitation was studied by Morello et. al. [82]. Consecutive PL acquisitions on single core–shell nanorods fabricated by the seeded growth method showed only small fluctuations of the

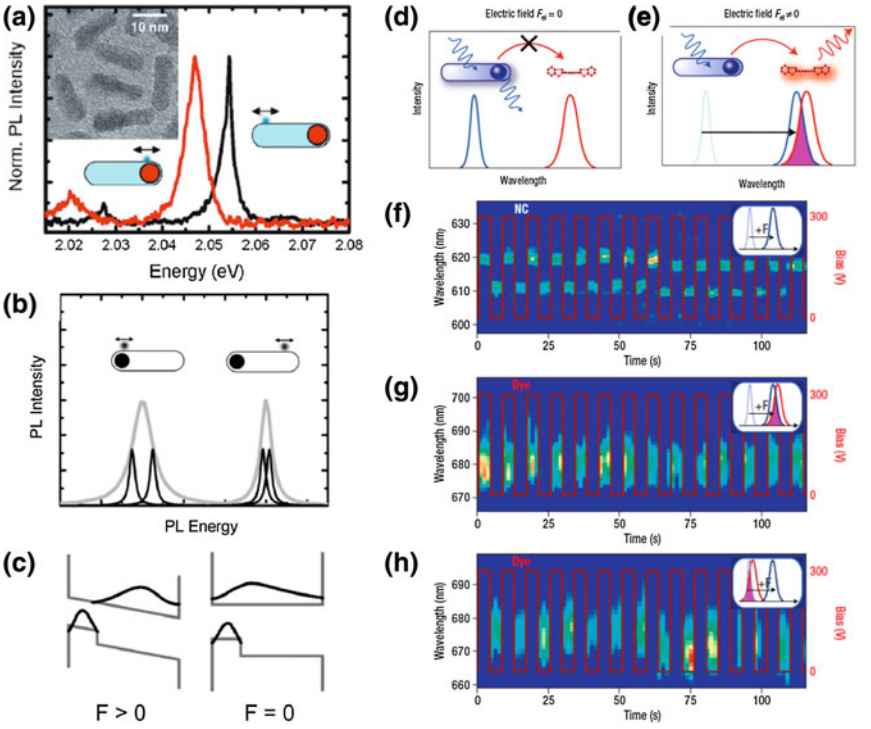

Fig. 2.27 **a** Fluctuations in the emission energy recorded from single CdSe/CdS nanorods. Taken with permission from Ref. [76]. **b** Illustration of the origin of these fluctuations due to surface charges from Ref. [77]. **c** band bending induced by electric field. **d**, **e** Mechanism of Foerster energy transfer from nanorods to organic dyes, which is controlled by an external electric field. **f** Switching of the PL of single nanorods by an external electric field. **g**, **h** Switching the emission of nanocrystal-dye couples on and off by an external electric field for two different nanocrystal-dye combinations. Taken with permission from Ref. [121]

energetic position (of the order of a few meV) due to the spectral diffusion, which was indicative of a low level of surface charge fluctuations. However, an increase in the excitation density resulted in a systematic blue-shift of the emission peak, which varied in the range from 15 to 35 meV for different rods (see Fig. 2.29c). The reversibility of the experiment implied that this shift could be considered as an intrinsic property, rather than due to some photo-degradation process. Figure 2.29d shows power-dependent PL positions taken at different temporal delays. Here, 2 $\mu J/cm^2$ refers to an excitation density corresponding to a low excitation regime (less than one photogenerated e–h pair per rod), whereas at higher densities the system is in the multiexciton generation regime. A noticeable dynamical red-shift occurred in the multiexcitonic regime (with a maximum shift of 25 meV measured at excitation density of 107 $\mu J/cm^2$), in contrast to the almost constant temporal PL position featuring the low density excitation measurement.

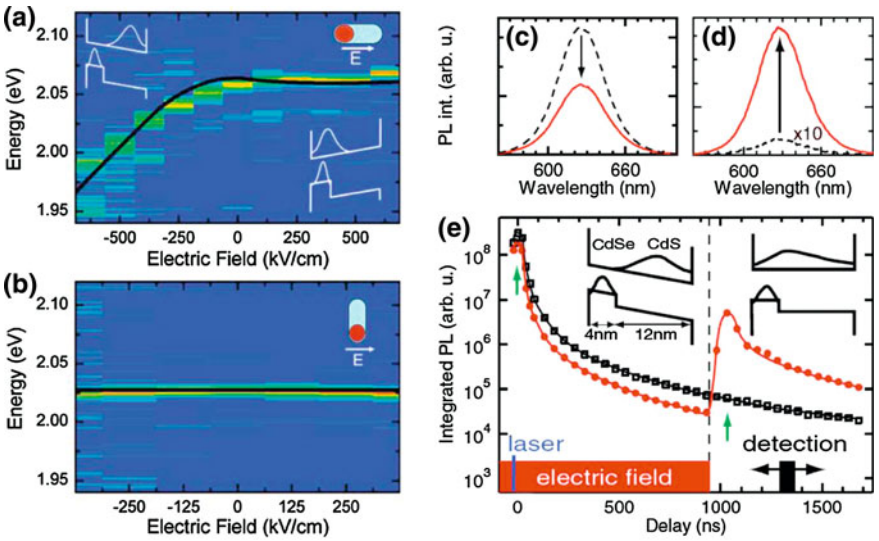

Fig. 2.28 **a**, **b** Energy shift of the emission peak of a single CdSe/CdS nanorod induced via the Stark effect by an external electric field. In **a** the e-field is oriented parallel to the long axis of the rod, and in **b** is perpendicular. **a**, **b** are taken with permission from Ref. [53]. **c**, **d** Electrical exciton storage in semiconductor nanocrystals at room temperature. **c** Prompt emission spectrum recorded in a 50 ns window overlaying excitation with (*solid line*) and without (*dashed line*) an electric field pulse. **d** As in **c** but with the detection placed 1.03 μs after excitation following the 1 μs field pulse. In this case the stored excitons result in a luminescence flash. **e** Time resolved PL decay with (*full circles*) and without (hollow squares) an electric field pulse of 1 μs duration. The arrows show the times of recording the spectra in **c** and **d**. The sketches indicate the separation of electron and hole wave functions during and after application of the field. **c**–**e** are taken with permission from Ref. [81]

A transient red-shift resulting from the photo-induced dynamical de-screening of an internal electric field is a commonly observed process in a number of systems exhibiting internal electric fields. For example, in GaN-based systems [83, 84] the piezoelectric nature of the material gives rise to a polarization that originates from the lattice strain at the GaN/AlN interface. We note that the lattice mismatch at the GaN/AlN interface is comparable to that of CdSe/CdS heterostructures (of the order of 4.1 % [66, 78, 82]). In addition to the screening of an internal field, another possible reason for the blue-shifted high power spectra could be of bi-excitonic origin. However, theoretical calculations allowed to rule out the biexciton emission as cause of the observed nonlinearity [82].

Another appealing property of CdSe/CdS core–shell nanorods is that they can act as single photon sources. An experimental proof for single photon emission is to measure the coincidence of the emitted photons in a high sensitivity Hanbury Brown and Twiss setup based on two avalanche photodetectors [85]. For single photon emitters the coincidence histogram shows negligible counts at zero delay time, an effect that is called photon anti-bunching [86, 87], in contrast to the

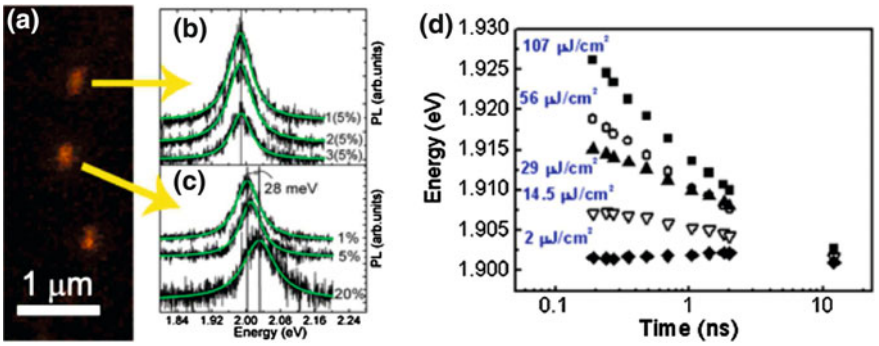

Fig. 2.29 **a** Image of a random field of single nanorods acquired by scanning the sample across a diffraction-limited laser spot of a confocal microscope. The sample was prepared by drop casting a nanomolar nanorod solution onto a cover glass and by rapidly blowing off the solution by means of a strong nitrogen flow. **b** Spectra collected consecutively from a single rod (*black lines*) (identified by the arrow in panel **a**) obtained at the same laser power, and relative Lorentzian best fit curves (*green lines*). **c** PL spectra from a single rod (*black lines*) (indicated by arrow in panel **a**) obtained by varying the excitation power, from 1 to 20 % of the maximum available power (1 mW), and relative Lorentzian best fit curves (*green lines*) Taken with permission from Ref. [82]. **d** Transient emission energies measured at different delays after the excitation, recorded at excitation densities ranging from 2 $\mu J/cm^2$, at which no shift was observed, to the maximum value (107 $\mu J/cm^2$) allowed by the experimental set-up. Taken with permission from Ref. [82]

photon bunching that occurs in the emission of thermal light sources due to the boson nature of photons. Pisanello et al. [88] investigated the potential of single core–shell nanorods as fully polarized single photon sources operating at room temperature, and confirmed also the spatial directionality of the nanorod emission, which resembles the emission geometry of a dipole antenna (Fig. 2.30).

2.7.4 Type-I and Type-II Transitions in CdSe/CdS Nanorods

For bulk and superlattice structures the band alignment at the CdSe/CdS interface is of type-I [89, 90]. However, for nanostructures this might be different due to quantum confinement effects. For holes the bulk valence band-offset is of about 0.8 eV, which is too large to be inverted by quantization effects, especially if we consider the higher effective mass of the holes with respect to the electrons. In the conduction band, on the other hand, it is possible to have a positive or negative band-offset, depending on the quantization energy in the core. Indeed, the reported values span the large range from −0.25 to +0.27 eV [63]. So far the most practical way to describe CdSe/CdS dot/rod heterostructures has been to assume a zero conduction band-offset [53, 77], thus implying a quasi-type-II structure, provided that the experimental results could be well explained. The possibility of tuning the core size in these nanostructures, using the so-called “seeded growth” approach

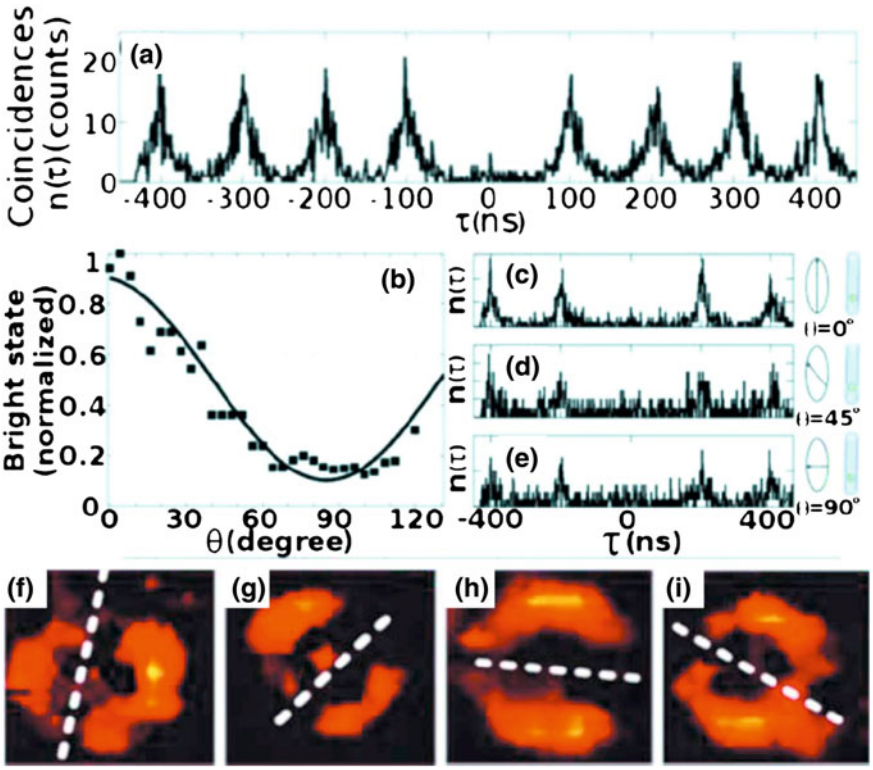

Fig. 2.30 **a** Antibunching of the single nanorod emission. **b** Normalized PL amplitude versus polarization angle of a single nanorod. **c–e** Antibunching traces relative to three different emission polarizations. **f–i** Spatially resolved emission of single nanorods by defocalized emission measurements in a confocal microscope. Taken with permission from Ref. [88]

[64] has allowed to study the conduction band offsets in these core/shell nanorods in more detail.

As was discussed earlier in this section, many optical experiments can be well explained by a flat conduction band profile, whereas electrical studies by scanning probe spectroscopy have revealed a pronounced confinement of the electrons in the core region (see also Chap. 3 on electrical properties). This contradiction has been resolved recently by a work of Banin et al. [91], in which a systematic PL and absorption study on nanorods with different core and shell sizes has shown that the electron delocalization is strongly sensitive to the core size. In detail, the lowest level in the conduction band is localized in the core for large core sizes (in that work this meant diameters above 2.8 nm) and the system behaves like a type-I structure, whereas for smaller cores the quantum confinement raises the energy of this level above the conduction band minimum of the shell. The experimental evidence of such behavior was obtained by varying the excitation density of an ensemble of rods. In general, at low excitation density (corresponding to a

generation of less than one e–h pair per rod) only one PL peak was observed and was associated to single exciton emission. With increasing excitation power density (up to three orders of magnitude) additional peaks gradually appeared, which were ascribed to biexciton and triexciton emission (in order of apparition). Banin et al. found that depending on the core size the biexciton PL may be red- or blue-shifted with respect to the single exciton energy. This shift provides a measure of the biexciton binding energy, which is different in type-I and type-II systems. The biexciton is composed of four carriers (two electrons and two holes), which in a type-I structure are distributed in the same spatial region, whereas in type-II structure electrons and holes are spatially separated into different regions. The result is depicted in Fig. 2.31. When the four carriers reside in the same material, they can distribute in order to minimize the Coulomb interaction among them, resulting in an energetically favorable bound biexcitonic system. The binding energy is thus negative and the consequent emission is red-shifted with respect to the single exciton PL (Fig. 2.31, left panel).

On the contrary, in a type-II configuration only carriers having the same charge reside in the same spatial region, as they are obliged to do so by the particular conduction and valence band-offset (Fig. 2.31, right panel). The result is that the Coulomb interaction between the charge carriers is not minimized, thus a blue-shift with respect to the exciton energy is predicted and is actually measured in several nanostructures [44, 45].

Figure 2.32 shows the optical spectra for nanorods with a large (a) and small (b) core size, and summarizes the results obtained by Banin and co-workers on CdSe/CdS nanorods having different core diameters [91]. For core diameters larger than 2.8 nm the biexcitonic peak was red-shifted with respect to the single exciton peak and for diameters smaller than 2.8 nm the relative positions of the exciton and biexciton were inverted, indicating the shift from a type-I to a type-II system (see Fig. 2.32c).

Recent photoluminescence studies have revealed a partial temperature-dependent delocalization of the electron wavefunction into the CdS shell, independently from the core size. In particular, Rain al. [92] have found evidence for an increase

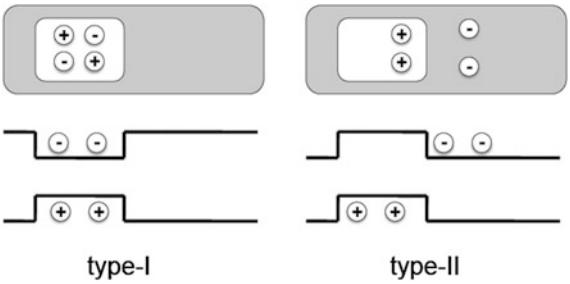

Fig. 2.31 Sketch of the biexciton system in type-I and type-II heterostructures. In type-I structures the four photogenerated charges reside in the same material in a quadrupole configuration. The type-II materials constrain just the charges having the same sign to stay in the same materials, giving rise to an unfavorable energetic configuration for the biexciton

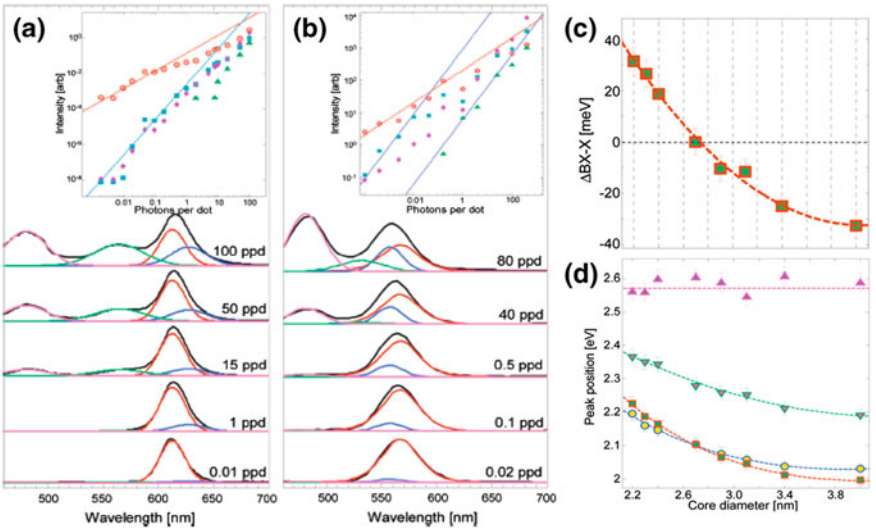

Fig. 2.32 **a** Transient emission spectra (*solid black line*) measured at the peak of the excitation pulse at increasing pulse energies ranging from 0.01 to 150 photon per dot (ppd) **a** for 4 nm diameter CdSe cores embedded in 45 × 6 nm CdS rods, **b** for 2.2 nm diameter CdSe cores embedded in 114 × 4.7 nm CdS rods. **c** Plot of the difference between the biexciton and exciton energetic positions for CdSe/CdS nanorods as function of the seed diameter. The crossover from negative values (attractive biexciton binding energy) to positive energies (repulsive biexciton binding energy) constitutes a fingerprint of the transformation of the system from type-I to type-II. **d** multiexciton peaks as function of the core dimensions: exciton (*circles*), biexciton (*squares*), triexciton (*downward-pointing triangles*) and CdS exciton (*triangles*). The crossover involving exciton and biexciton is noticeable. Taken with permission from Ref. [91]

in lifetime that was ascribed to thermal electron delocalization, corroborating the previously discussed findings of pump-probe experiments and recent femtosecond cross-polarized transient grating studies [93]. At the same time the PL energy and broadening followed a classical thermal behavior referable to type-I semiconductors, and the extracted physical parameters of the emitting species like Debye temperature and optical phonons energies were ascribable to the CdSe core material [92], pointing toward a major role of the electron delocalization only on what concerns the radiative rate of CdSe/CdS nanorods.

2.7.5 Optical Properties of Ordered Nanorod Assemblies

As discussed earlier in this section, the advent of the seeded growth approach for the fabrication of core–shell nanorods has significantly improved the quality of the nanorod samples in terms of monodispersity, line width of the emission, and quantum yield [64]. This new synthesis technique, where the seed is fabricated and size selected in a prior step, has boosted the progress on assembly of anisotropic

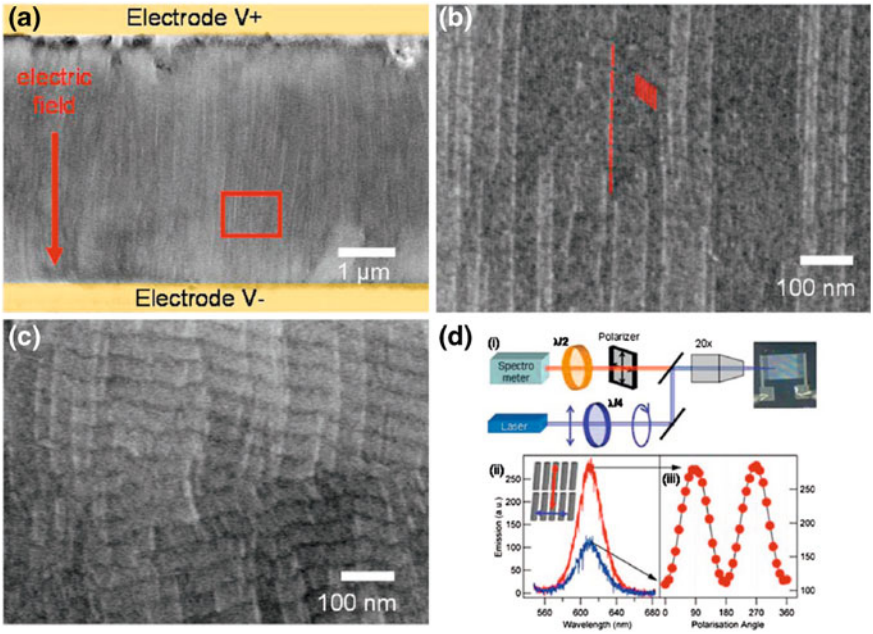

Fig. 2.33 **a–c** SEM images of nanorods aligned by means of electric fields. **d** Schematic illustration of the setup (*i*) employed for the polarization measurements and relative results (*ii*, *iii*). Spectra in (*ii*) show the emission polarized parallel (*red signal*) and perpendicularly (*blue signal*) to the alignment direction. Panel (*iii*) show the PL versus the polarization angle (*red symbols*) fitted to a $\cos^2$ function (*black line*). Taken with permission from Ref. [64]

nanocrystals, on the study of optical properties of such assemblies, and additionally on the fabrication of branched nanocrystals [91, 94, 95]. An interesting feature of nanorods with uniform lengths and diameters consists in the possibility to align them over large areas [64, 96, 97]), as shown in Fig. 2.33. Confocal spectroscopy made it possible to optically characterize regions of nanorods aligned according to various geometries with respect to a substrate, namely lateral, vertical and random. As one example, arrays of laterally aligned CdSe/CdS nanorods exhibited linearly polarized emission approaching a degree of polarization of 80 % [63, 88]. Figure 2.33 shows scanning electron microscopy (SEM) images of laterally aligned nanorods, and the polarized signal originating from those areas.

Figure 2.34 reports the spatially resolved PL spectra collected from regions showing different types of nanorod alignment [64]. Measurements on regions of rods vertically oriented with respect to the substrate were almost non emissive in the vertical direction and the weak PL was slightly blue-shifted (a few meV) with respect to the more intense signal originating from disordered nanorods. A more pronounced blue-shift (up to 30 meV) and much higher intensity of the PL were noticeable on lateral assemblies. The difference in PL intensity between laterally- and vertically-aligned nanorods could be ascribed to the spatial anisotropy of the optical dipole emission

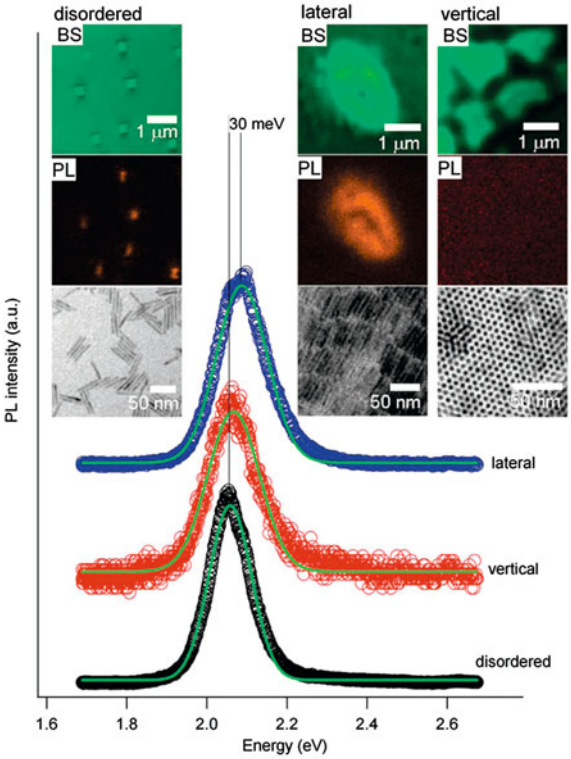

Fig. 2.34 (Main panel): PL from region of laterally-, vertically-aligned and disordered nanorods with relative Gaussian best fit curves (*green lines*). Upper panels show TEM, PL and backscattering images from the same regions. Taken with permission from Ref. [64]

in nanorods. The transition dipole in such nanorods is parallel to the rod long axis, thus the PL intensity is expected to be maximal in the plane perpendicular to the dipole and minimal in the direction of the long axis. The unexpected behavior consists in the energy shift, and a possible explanation of this effect is the screening of an internal (piezo) electric field present in the individual nanorods due to the photogenerated charge distributions in neighboring rods (as discussed in detail earlier).

The possibility to organize nanorods into ordered arrays on micrometer and millimeter length scales makes them an interesting material for macroscopic optical applications. As an example, Rizzo et al. fabricated a polarized light emitting diode based on an array of laterally oriented nanorods [98]. Also, nanorods can be employed as active material for lasing devices. Here, typically, the emitting medium is embedded in an external resonator for optical feedback [99–101]. A novel approach for self assembled micro-lasers was proposed recently by Zavelani et al. [102, 103]. Here the coffee stain effect that governs the microfluidic dynamics in an evaporating droplet [104, 105] led to the formation of well-defined stripes that consisted of densely packed, laterally aligned nanorods. The borders of these stripes were sharp and smooth enough to form a resonant cavity that was able to sustain laser emission both from core- and shell transitions of the nanorods [103], as can be seen in Fig. 2.35.

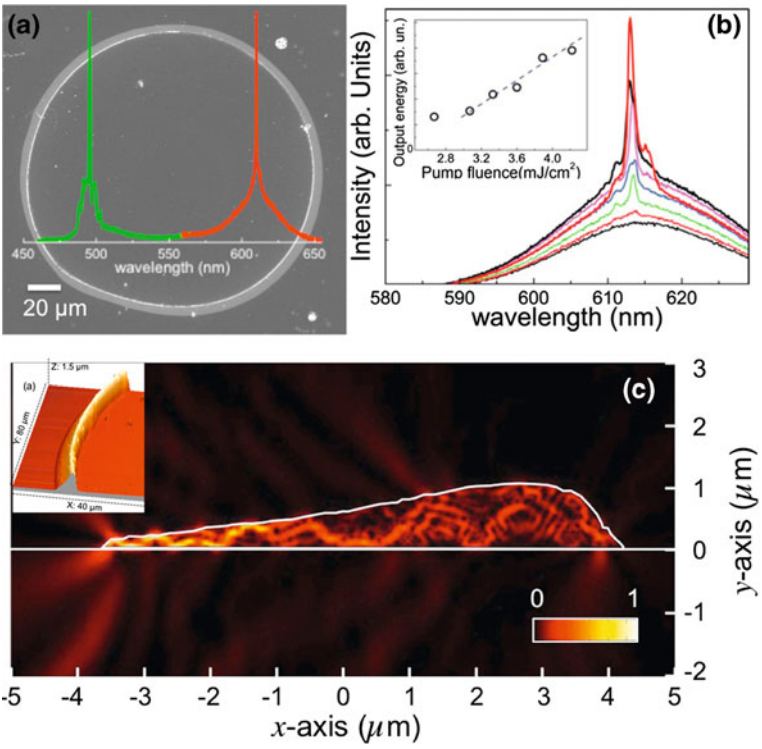

Fig. 2.35 Lasing from self-assembled nanorod cavities. **a** Scanning electron microscope (SEM) image of the coffee stain deposit formed by jet deposition of a solution of nanorods dissolved in toluene, overlaid with laser emission spectra in the red and green. The borders of the coffee stain ring are well defined and function as a resonant cavity able to sustain lasing. **b** Emission from a coffee stain nanorod deposit for different pump excitation intensities, the inset shows the linear input-out typical for laser action. Taken with permission from Ref. [102]. **c** Finite elements modeling of the resonant modes sustained by a cavity with a cross section corresponding to the shape that was obtained by atomic-force microscopy measurements (*see inset*) on the coffee stain rings. Taken with permission from Ref. [122]

2.7.6 Collinear Nanorods and Nanobarbells

Collinear heterostructures exhibit a direct exposure of both materials of their surface and are interesting candidates for photovoltaic [65–70] and photocatalytic [71–73] applications (see also Chapter 6). Among the type-II rod-like systems, CdSe/CdTe has the advantages of a well controlled synthesis and small lattice mismatch between the two materials. Therefore it is the most studied heterostructure with type-II band-alignment [68–70, 72, 106, 107]. Optical investigation techniques including steady-state (absorption and PL measurements) and time-resolved spectroscopy allow to monitor effectively the carrier dynamics and localization in these nanostructures. Figure 2.36 shows typical absorption and PL

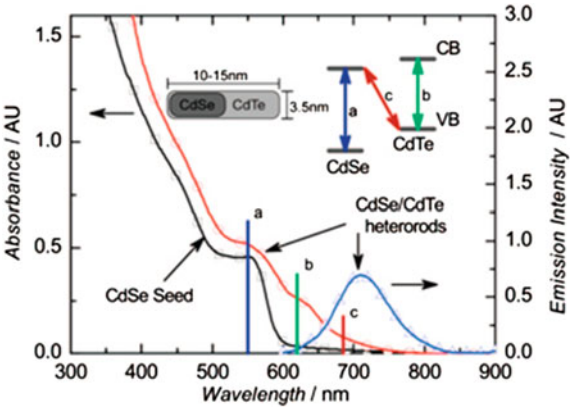

Fig. 2.36 Absorption and PL spectra of a representative coaxial CdSe/CdTe heterostructure. *Inset* sketch of the band-alignment and labeling of the transitions indicated on the rod absorption (*red line*). Taken with permission from Ref. [70]

spectra of collinear CdSe/CdTe nanorods. The absorption spectra show features arising from a superposition of the single sections that constitute the heterostructure, whereas the PL signal occurs at an energy that is well below the band gap of the single material sections, if these are considered separately.

In collinear nanorods the emission from the CdSe material is often observed as well, but with a strongly reduced intensity with respect to the core–shell or tetrapod systems [68, 94, 107]. The presence of such visible emission has been ascribed to ultrafast hole transfer from the core to the outer material and/or to resonant energy transfer from seeds having band gap larger than the shell [107]. Further evidence of the real nature of the detected PL signal is usually obtained by analyzing the lifetime of both emission peaks. Due to the spatial separation of e–h wavefunctions, the radiative rate (proportional to the e–h wavefunctions overlap) is strongly reduced with respect to a type-I optical transition. This is reflected in time-resolved measurements showing type-II PL lifetime ranging from few hundreds of nanoseconds to some microseconds against the more classical PL decay on the nanosecond timescale observed in type-I transitions [106–108].

Collinear nanorods are preferred in the study of the fundamental physical properties, since it is possible to discern the role of core and shell in the absorption process. This allowed to precisely determine the dynamics of charge carriers after generation by means of pump-probe technique. Transient absorption measurements performed by Dooley and co-workers have disclosed the real carrier pathways finding an ultrafast charge separation on the 500 fs timescale [70]. The noteworthy characteristic of these systems, apart from the type-II transition, is the presence of a PL peak falling in the visible range and referable to radiative emission of the outer material (see for instance Fig. 2.36) [68, 69, 107].

Differently from some collinear and dot/rod systems, where an internal seed material is always buried in an outer material having the role of both charge separator and passivating agent, nanobarbells are characterized by having a second component deposited only on the tips of the rod (see Fig. 2.22) [72, 73]. Apart from the geometry, a fundamental difference with respect to the structures previously described lies in the role of the second material. Nanobarbells are of

potential interest for photocatalysis, where both the separated charges have to be readily available for chemical reactions, since both material components are directly exposed to the ambient conditions.

This specific geometry has also strong implications on the optical properties of the overall nanocrystal, since the second material does not grow as a passivating uniform layer on top of the starting rod. Indeed, the most common behavior in these structures consists in a drastic change of the luminescence performances, mainly due to trapping processes occurring on the surface of both exposed components. Depending on the material, the effect may correspond to an increase or decrease of the performances. Figure 2.37 shows an example of what happens for two different systems, CdSe/CdTe and ZnSe/CdS [72, 73]. In the CdSe/CdTe nanobarbells the PL is quenched after deposition of CdTe on the CdSe rod, which makes them ideal structures in photocatalytic applications (see Fig. 2.37a). On the contrary, the PL signal coming from ZnSe/CdS system transforms from a broad, trap related emission of CdS rods to a sharper, more intense signal falling in the same spectral range (Fig. 2.37b).

2.7.7 *Multifunctional Nanorods*

The advent of synthesis approaches allowing for narrow distributions of the geometric parameters of colloidal nanocrystals has directed the research towards the fabrication of more elaborate multi-component nanostructures, which in principle would be able to fulfill multiple tasks simultaneously. In particular, the combination of magnetic and optical properties is attractive for application of such nanocrystals as bio-labeling and analytical separation, drug delivery or multimodal diagnostics and therapeutics. Among the several colloidal nanostructures that have

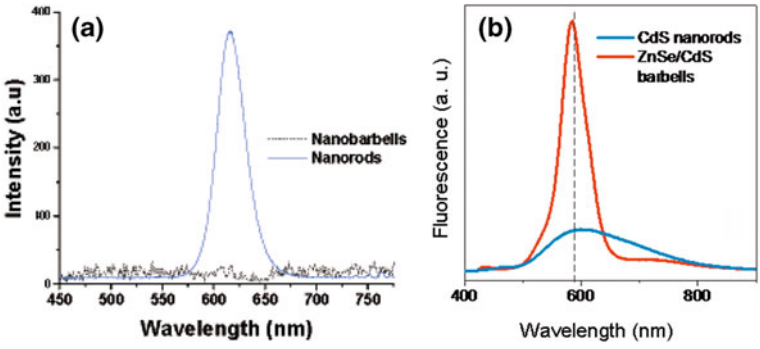

Fig. 2.37 **a** Collapse of the CdSe/CdTe nanobarbells PL respect to the starting CdSe nanorods. Taken with permission from Ref. [72]. **b** Comparison between PL coming from CdS nanorods (*blue line*) and ZnSe/CdS nanobarbells (*red line*) showing increased efficiency. Taken with permission from Ref. [73]

been reported in the last years (and not limited to nanorods), we mention Co/CdSe core–shell nanocrystals [109], FePt-CdX (X = S, Se) heterodimers [110–113], γ-Fe_2O_3-MeX (Me = Cd, Zn, Hg and X = S, Se) heterodimers [114–116], CdSe/CdS, and CdSe nanorods decorated with PtNi/PtCo or Co domains [75, 117]. All these structures have been fabricated with the initial goal to "pack" into a single nanostructure magnetic and optical properties, although the final outcome has not always been very successful.

For what concerns nanorods for example, the basic idea in this direction is to grow other materials with optical/magnetic properties selectively at their tip regions. Unfortunately a common fate of metal-tipped nanorods is the drastic drop of their PL quantum yield (PL QY), due to fast semiconductor–metal charge transfer. However, the last generation of seeded grown CdSe/CdS nanorods (having a starting QY approaching 70 % at room temperature) offers the opportunity to preserve larger efficiency after semiconductor–metal coupling. Recently, fluorescent Co-tipped CdSe/CdS dot/rod heterostructures exhibiting ferromagnetic behavior at room temperature have been successfully reported [74]. In Fig. 2.38 we show an image of these Co-tipped nanorods, obtained by energy-filtered TEM (EFTEM). In the sample, which has been imaged before separation of the metal-tipped nanorods from unreacted rods, one can see clearly the selective growth of Co domains only on one tip region of individual rods, and in few cases the analysis allowed to identify this tip region as being far from the region of the CdS rod in which the initial CdSe was buried (for more details, see Ref. [74]). Figure 2.39a shows the optical absorption and emission spectra of the initial CdSe cores (i.e. the "seeds") of the CdSe/CdS nanorods, of physical mixtures of Co nanocrystals and CdSe/CdS nanorods, and finally of Co-tipped nanorods (the latter obtained after magnetic separation, hence containing a negligible amount of non-reacted nanorods). As discussed previously, the absorption from CdSe/CdS

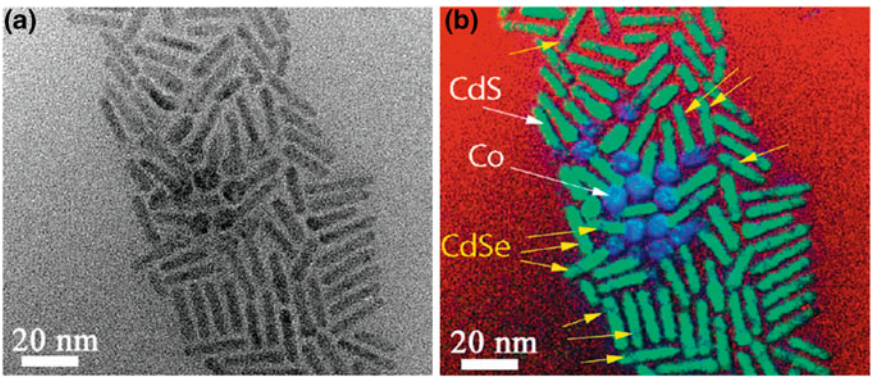

Fig. 2.38 **a** Elastic zero-loss EFTEM image of a sample of Co-tipped nanorods. **b** Composite false-color image obtained from **a** showing the different domains of the sample. CdS rod (*green*), cobalt domains (*blue spheres* on the tips of the rods), CdSe cores (*blue* zones inside the CdS rods). Taken with permission from Ref. [74]

nanorods presents a sharp profile in correspondence of the CdS excitonic absorption (about 495 nm) and a smooth behavior at longer wavelengths, where a weak CdSe absorption can be detected.

The relative PL emission clearly falls in the CdSe spectral domain, indicating a type-I recombination in the cores, and is slightly red-shifted (together with the lowest absorption peak) with respect to the starting seeds counterpart. This behavior, largely observed in heterostructures, is ascribed in this case to the electron wavefunction spreading, which leads to the observed red-shifts. The physical mixture of rods and Co particles has an absorption spectrum that reproduces a linear combination of the two systems considered, and a PL typical of the nanorods, with a PL quantum yield of about 25 %.

On the contrary, Co-tipped nanorods present an almost flat absorption as a consequence of the effective electronic coupling between the two components. Their PL QY, despite being only around 3 %, is nevertheless the highest efficiency reported so far for semiconductor-magnetic nanocrystals in which the two domains are directly bound to each other (i.e. without any molecule/polymer acting as a spacer between them). The reduction of the PL QY is explained in terms of fast charge transfer from the semiconductor to the metal particles and has been investigated by time resolved spectroscopy (see Fig. 2.39b). The PL from the CdSe/CdS nanorods decays in about 12 ns, whereas in a physical mixture of CdSe/CdS nanorods and Co nanoparticles the lifetime is about 7 ns. On the other hand, the Co-tipped rods exhibits a time constant of only 350 ps. Considering that these

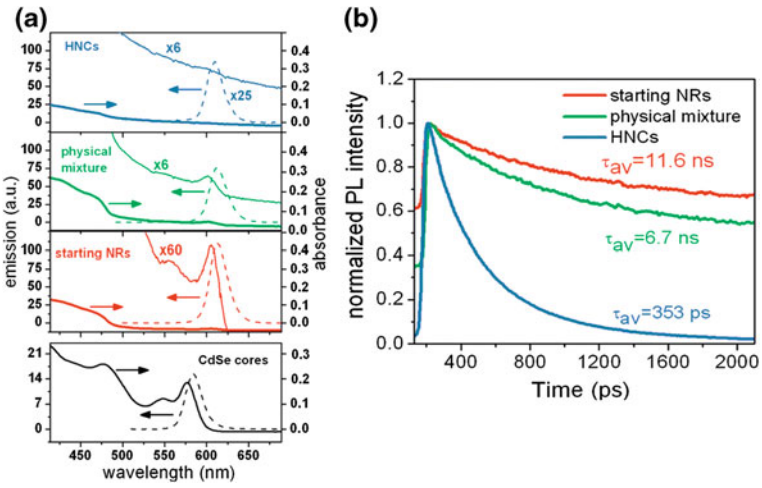

Fig. 2.39 **a** Series of absorption (*continuous lines*) and PL spectra (*dashed lines*) of starting CdSe cores (*black lines*), CdSe/CdS nanorods (*red lines*), a physical mixture of Co nanoparticles and CdSe/CdS nanorods (*green lines*), Co-tipped nanorods (*blue lines*). **b** Time traces of the PL recorded at room temperature on starting CdSe/CdS nanorods (*red line*), physical mixture of Co nanoparticles and CdSe/CdS nanorods (*green line*), Co-tipped nanorods (*blue line*). Taken with permission from Ref. [74]

three systems undergo a progressive decrease of their PL QY, the reduction of the lifetime cannot be ascribed to an increased radiative recombination rate (which would lead to a progressive increase of the PL efficiency). Instead, the reduction in lifetime in Co-tipped nanorods can be attributed to an increase of the non-radiative rate, due to the rapid charge transfer induced by the electronic communication between the semiconductor material and the cobalt domain attached to it. For the mixture of CdSe/CdS nanorods and Co nanoparticles, in which no direct Co-nanorod interface is present, the moderate decrease in the decay time can be ascribed to the activation of non-radiative channels different from charge transfer. Most likely, these are due to energy transfer from semiconductor to metal, as already observed in similar systems [118]. Despite the large reduction of the emission efficiency in Co-tipped nanorods, some detectable PL signal remains, which makes such heterostructures promising candidates as active media in optical/magnetic applications.

References

1. Schmelcher P (1993) Delocalization of excitons in a magnetic-field. Phys Rev B 48(19):14642–14645
2. Efros AL, Rosen M (2000) The electronic structure of semiconductor nanocrystals. Annu Rev Mater Sci 30:475–521
3. Ekimov AI, Onushchenko AA, Efros AL (1986) JETP Lett 43:376
4. Ekimov AI, Efros AL, Ivanov MG, Onushchenko AA, Shumilov SK (1989) Donor-like exciton in zero-dimension semiconductor structures. Solid State Commun 69(5):565–568
5. Li JB, Wang LW (2003) Shape effects on electronic states of nanocrystals. Nano Lett 3(10):1357–1363
6. Shabaev A, Efros AL (2004) 1D exciton spectroscopy of semiconductor nanorods. Nano Lett 4(10):1821–1825
7. Efros AL, Rosen M, Kuno M, Nirmal M, Norris DJ, Bawendi M (1996) Band-edge exciton in quantum dots of semiconductors with a degenerate valence band: dark and bright exciton states. Phys Rev B 54(7):4843–4856
8. Norris DJ, Efros AL, Rosen M, Bawendi MG (1996) Size dependence of exciton fine structure in CdSe quantum dots. Phys Rev B 53(24):16347–16354
9. Nirmal M, Norris DJ, Kuno M, Bawendi MG, Efros AL, Rosen M (1995) Observation of the dark exciton in CdSe quantum dots. Phys Rev Lett 75(20):3728–3731
10. Le Thomas N, Herz E, Schops O, Woggon U, Artemyev MV (2005) Exciton fine structure in single CdSe nanorods. Phys Rev Lett 94(1):016803
11. Le Thomas N, Allione M, Fedutik Y, Woggon U, Artemyev MV, Ustinovich EA (2006) Multiline spectra of single CdSe/ZnS core-shell nanorods. Appl Phys Lett 89(26):263115
12. Lange H, Machon M, Artemyev M, Woggon U, Thomsen C (2007) Effect of ZnS shell on the Raman spectra from CdSe nanorods. Phys Stat Sol Rap Res Lett 1(6):274–276
13. Artemyev M, Moller B, Woggon U (2003) Unidirectional alignment of CdSe nanorods. Nano Lett 3(4):509–512
14. Talaat H, Abdallah T, Mohamed MB, Negm S, El-Sayed MA (2009) The sensitivity of the energy band gap to changes in the dimensions of the CdSe quantum rods at room temperature: STM and theoretical studies. Chem Phys Lett 473(4–6):288–292
15. Katz D, Wizansky T, Millo O, Rothenberg E, Mokari T, Banin U (2002) Size-dependent tunneling and optical spectroscopy of CdSe quantum rods. Phys Rev Lett 89(8):086801

16. Millo O, Katz D, Steiner D, Rothenberg E, Mokari T, Kazes M, Banin U (2004) Charging and quantum size effects in tunnelling and optical spectroscopy of CdSe nanorods. Nanotechnology 15(1):R1–R6
17. Hu JT, Li LS, Yang WD, Manna L, Wang LW, Alivisatos AP (2001) Linearly polarized emission from colloidal semiconductor quantum rods. Science 292(5524):2060–2063
18. De Giorgi M, Lingk C, von Plessen G, Feldmann J, De Rinaldis S, Passaseo A, De Vittorio M, Cingolani R, Lomascolo M (2001) Capture and thermal re-emission of carriers in long-wavelength InGaAs/GaAs quantum dots. Appl Phys Lett 79(24):3968–3970
19. Morello G, De Giorgi M, Kudera S, Manna L, Cingolani R, Anni M (2007) Temperature and size dependence of nonradiative relaxation and exciton-phonon coupling in colloidal CdTe quantum dots. J Phys Chem C 111(16):5846–5849
20. Valerini D, Creti A, Lomascolo M, Manna L, Cingolani R, Anni M (2005) Temperature dependence of the photoluminescence properties of colloidal CdSe/ZnS core/shell quantum dots embedded in a polystyrene matrix. Phys Rev B 71(23):235409
21. Klimov VI, Mikhailovsky AA, McBranch DW, Leatherdale CA, Bawendi MG (2000) Quantization of multiparticle Auger rates in semiconductor quantum dots. Science 287(5455):1011–1013
22. Fisher B, Caruge JM, Zehnder D, Bawendi M (2005) Room-temperature ordered photon emission from multiexciton states in single CdSe core-shell nanocrystals. Phys Rev Lett 94(8):087403
23. Pandey A, Guyot-Sionnest P (2007) Multicarrier recombination in colloidal quantum dots. J Chem Phys 127(11):111104
24. Achermann M, Hollingsworth JA, Klimov VI (2003) Multiexcitons confined within a subexcitonic volume: spectroscopic and dynamical signatures of neutral and charged biexcitons in ultrasmall semiconductor nanocrystals. Phys Rev B 68(24):245302
25. Wang LW, Califano M, Zunger A, Franceschetti A (2003) Pseudopotential theory of Auger processes in CdSe quantum dots. Phys Rev Lett 91(5):056404
26. Kraus RM, Lagoudakis PG, Muller J, Rogach AL, Lupton JM, Feldmann J, Talapin DV, Weller H (2005) Interplay between auger and ionization processes in nanocrystal quantum dots. J Phys Chem B 109(39):18214–18217
27. Klimov VI (2000) Optical nonlinearities and ultrafast carrier dynamics in semiconductor nanocrystals. J Phys Chem B 104(26):6112–6123
28. Achermann M, Bartko AP, Hollingsworth JA, Klimov VI (2006) The effect of Auger heating on intraband carrier relaxation in semiconductor quantum rods. Nat Phys 2(8):557–561
29. Htoon H, Hollingsworth JA, Dickerson R, Klimov VI (2003) Effect of zero- to one-dimensional transformation on multiparticle Auger recombination in semiconductor quantum rods. Phys Rev Lett 91(22):227401
30. Robel I, Bunker BA, Kamat PV, Kuno M (2006) Exciton recombination dynamics in CdSe nanowires: bimolecular to three-carrier Auger kinetics. Nano Lett 6(7):1344–1349
31. Liebler JG, Schmitt-Rink S, Haug H (1985) Theory of the absorption tail of wannier excitons in polar semiconductors. J Lumin 34:1–7
32. Takagahara T (1996) Electron-phonon interactions in semiconductor nanocrystals. J Lumin 70:129–143
33. Schmitt-Rink S, Miller DAB, Chemla DS (1987) Theory of the linear and nonlinear optical properties of semiconductor nanocrystallites. Phys Rev B 35:8113–8125
34. Nomura S, Kobayashi T (1992) Exciton-LO-phonon couplings in spherical semiconductor microcrystallites. Phys Rev B 45:1305–1316
35. Muljarov EA, Zimmermann R (2007) Exciton dephasing in quantum dots due to LO-phonon coupling: An exactly solvable model. Phys Rev Lett 98(18):187401
36. Gindele F, Hild K, Langbein W, Woggon U (2000) Temperature-dependent line widths of single excitons and biexcitons. J Lumin 87–89:381–383
37. Rudin S, Reinecke TL, Segall B (1990) Temperature-dependent exciton linewidths in semiconductors. Phys Rev B 42(17):11218–11231

38. Lange H, Artemyev M, Woggon U, Niermann T, Thomsen C (2008) Experimental investigation of exciton-LO-phonon couplings in CdSe/ZnS core/shell nanorods. Phys Rev B 77(19):193303
39. Trallero-Giner C, Debernardi A, Cardona M, Menendez-Proupin E, Ekimov AI (1998) Optical vibrons in CdSe dots and dispersion relation of the bulk material. Phys Rev B 57(8):4664–4669
40. Lange H, Artemyev M, Woggon U, Thomsen C (2009) Geometry dependence of the phonon modes in CdSe nanorods. Nanotechnology 20(4):045705
41. Nobile C, Kudera S, Fiore A, Carbone L, Chilla G, Kipp T, Heitmann D, Cingolani R, Manna L, Krahne R (2007) Confinement effects on optical phonons in spherical, rod-, and tetrapod-shaped nanocrystals detected by Raman spectroscopy. Phys Status Solidi A-Appl Mat 204(2):483–486
42. Gupta R, Xiong Q, Mahan GD, Eklund PC (2003) Surface optical phonons in gallium phosphide nanowires. Nano Lett 3(12):1745–1750
43. Krahne R, Chilla G, Schuller C, Carbone L, Kudera S, Mannarini G, Manna L, Heitmann D, Cingolani R (2006) Confinement effects on optical phonons in polar tetrapod nanocrystals detected by resonant inelastic light scattering. Nano Lett 6(3):478–482
44. Klimov VI, Ivanov SA, Nanda J, Achermann M, Bezel I, McGuire JA, Piryatinski A (2007) Single-exciton optical gain in semiconductor nanocrystals. Nature 447(7143):441–446
45. Nanda J, Ivanov SA, Achermann M, Bezel I, Piryatinski A, Klimov VI (2007) Light amplification in the single-exciton regime using exciton–exciton repulsion in type-II nanocrystal quantum dots. J Phys Chem C 111(42):15382–15390
46. Efros AL, Kharchenko VA, Rosen M (1995) Breaking the phonon bottleneck in nanometer quantum dots—role of Auger-like processes. Solid State Commun 93(4):281–284
47. Creti A, Anni M, Rossi MZ, Lanzani G, Manna L, Lomascolo M (2007) Role of defect states on Auger processes in resonantly pumped CdSe nanorods. Appl Phys Lett 91(9):093106
48. Wang S, Querner C, Fischbein MD, Willis L, Novikov DS, Crouch CH, Drndic M (2008) Blinking statistics correlated with nanoparticle number. Nano Lett 8(11):4020–4026
49. Wang S, Querner C, Emmons T, Drndic M, Crouch CH (2006) Fluorescence blinking statistics from CdSe core and core/shell nanorods. J Phys Chem B 110(46):23221–23227
50. Krishnan R, Hahn MA, Yu ZH, Silcox J, Fauchet PM, Krauss TD (2004) Polarization surface-charge density of single semiconductor quantum rods. Phys Rev Lett 92(21):216803
51. Li XZ, Xia JB (2003) Effects of electric field on the electronic structure and optical properties of quantum rods with wurtzite structure. Phys Rev B 68(16):165316
52. Rothenberg E, Kazes M, Shaviv E, Banin U (2005) Electric field induced switching of the fluorescence of single semiconductor quantum rods. Nano Lett 5(8):1581–1586
53. Muller J, Lupton JM, Lagoudakis PG, Schindler F, Koeppe R, Rogach AL, Feldmann J, Talapin DV, Weller H (2005) Wave function engineering in elongated semiconductor nanocrystals with heterogeneous carrier confinement. Nano Lett 5(10):2044–2049
54. Li XZ, Xia JB (2002) Electronic structure and optical properties of quantum rods with wurtzite structure. Phys Rev B 66(11):115316
55. Chen X, Nazzal A, Goorskey D, Xiao M, Peng ZA, Peng XG (2001) Polarization spectroscopy of single CdSe quantum rods. Phys Rev B 64(24):245304
56. Rothenberg E, Ebenstein Y, Kazes M, Banin U (2004) Two-photon fluorescence microscopy of single semiconductor quantum rods: direct observation of highly polarized nonlinear absorption dipole. J Phys Chem B 108(9):2797–2800
57. Wang J, Gudiksen MS, Duan X, Cui Y, Lieber CM (2001) Highly polarized photoluminescence and photodetection from single indium phosphide nanowires. Science 293(5534):1455–1457
58. Persson MP, Xu HQ (2004) Giant polarization anisotropy in optical transitions of free-standing InP nanowires. Phys Rev B 70:161310
59. Costi R, Saunders AE, Banin U (2010) Colloidal hybrid nanostructures: a new type of functional materials. Angew ChemInt Edit 49(29):4878–4897

60. Carbone L, Cozzoli PD (2010) Colloidal heterostructured nanocrystals: synthesis and growth mechanisms. Nano Today 5(5):449–493
61. Donega CDM (2011) Synthesis and properties of colloidal heteronanocrystals. Chem Soc Rev 40(3):1512–1546. doi:10.1039/C0CS00055H
62. Lo SS, Mirkovic T, Chuang CH, Burda C, Scholes GD (2011) Emergent Properties Resulting from Type-II Band Alignment in Semiconductor Nanoheterostructures. Adv Mater 23(2):180–197. doi:10.1002/adma.201002290
63. Steiner D, Dorfs D, Banin U, Della Sala F, Manna L, Millo O (2008) Determination of band offsets in heterostructured colloidal nanorods using scanning tunneling spectroscopy. Nano Lett 8(9):2954–2958. doi:10.1021/nl801848x
64. Carbone L, Nobile C, De Giorgi M, Sala FD, Morello G, Pompa P, Hytch M, Snoeck E, Fiore A, Franchini IR, Nadasan M, Silvestre AF, Chiodo L, Kudera S, Cingolani R, Krahne R, Manna L (2007) Synthesis and micrometer-scale assembly of colloidal CdSe/CdS nanorods prepared by a seeded growth approach. Nano Lett 7(10):2942–2950
65. Koo B, Korgel BA (2008) Coalescence and interface diffusion in linear CdTe/CdSe/CdTe heterojunction nanorods. Nano Lett 8(8):2490–2496
66. He J, Lo SS, Kim JH, Scholes GD (2008) Control of exciton spin relaxation by electron-hole decoupling in type-II nanocrystal heterostructures. Nano Lett 8(11):4007–4013
67. Shieh F, Saunders AE, Korgel BA (2005) General shape control of colloidal CdS, CdSe, CdTe quantum rods and quantum rod heterostructures. J Phys Chem B 109(18):8538–8542
68. Kumar S, Jones M, Lo SS, Scholes GD (2007) Nanorod heterostructures showing photoinduced charge separation. Small 3(9):1633–1639
69. Saunders AE, Koo B, Wang XY, Shih CK, Korgel BA (2008) Structural characterization and temperature-dependent photoluminescence of linear CdTe/CdSe/CdTe heterostructure nanorods. ChemPhysChem 9(8):1158–1163
70. Dooley CJ, Dimitrov SD, Fiebig T (2008) Ultrafast electron transfer dynamics in CdSe/CdTe donor-acceptor nanorods. J Phys Chem C 112(32):12074–12076
71. Hewa-Kasakarage NN, Kirsanova M, Nemchinov A, Schmall N, El-Khoury PZ, Tarnovsky AN, Zamkov M (2009) Radiative recombination of spatially extended excitons in (ZnSe/CdS)/CdS heterostructured nanorods. J Am Chem Soc 131(3):1328–1334
72. Halpert JE, Porter VJ, Zimmer JP, Bawendi MG (2006) Synthesis of CdSe/CdTe nanobarbells. J Am Chem Soc 128(39):12590–12591
73. Kirsanova M, Nemchinov A, Hewa-Kasakarage NN, Schmall N, Zamkov M (2009) Synthesis of ZnSe/CdS/ZnSe nanobarbells showing photoinduced charge separation. Chem Mater 21(18):4305–4309
74. Deka S, Falqui A, Bertoni G, Sangregorio C, Poneti G, Morello G, De Giorgi M, Giannini C, Cingolani R, Manna L, Cozzoli PD (2009) Fluorescent asymmetrically cobalt-tipped CdSe@CdS Core@Shell nanorod heterostructures exhibiting room-temperature ferromagnetic behavior. J Am Chem Soc 131(35):12817–12828
75. Maynadie J, Salant A, Falqui A, Respaud M, Shaviv E, Banin U, Soulantica K, Chaudret B (2009) Cobalt growth on the tips of CdSe nanorods. Angew ChemInt Edit 48(10):1814–1817
76. Muller J, Lupton JM, Rogach AL, Feldmann J, Talapin DV, Weller H (2004) Monitoring surface charge movement in single elongated semiconductor nanocrystals. Phys Rev Lett 93(16):167402
77. Muller J, Lupton JM, Rogach AL, Feldmann J, Talapin DV, Weller H (2005) Monitoring surface charge migration in the spectral dynamics of single CdSe/CdS nanodot/nanorod heterostructures. Phys Rev B 72(20):205339
78. Lupo MG, Della Sala F, Carbone L, Zavelani-Rossi M, Fiore A, Luer L, Polli D, Cingolani R, Manna L, Lanzani G (2008) Ultrafast electron-hole dynamics in core/shell CdSe/CdS dot/rod nanocrystals. Nano Lett 8(12):4582–4587
79. Talapin DV, Nelson JH, Shevchenko EV, Aloni S, Sadtler B, Alivisatos AP (2007) Seeded growth of highly luminescent CdSe/CdS nanoheterostructures with rod and tetrapod morphologies. Nano Lett 7(10):2951–2959

80. Creti A, Anni M, Zavelani-Rossi M, Lanzani G, Leo G, Della Sala F, Manna L, Lomascolo M (2005) Ultrafast carrier dynamics in core and core/shell CdSe quantum rods: role of the surface and interface defects. Phys Rev B 72(12):125346
81. Kraus RM, Lagoudakis PG, Rogach AL, Talapin DV, Weller H, Lupton JM, Feldmann J (2007) Room-temperature exciton storage in elongated semiconductor nanocrystals. Phys Rev Lett 98(1):017401
82. Morello G, Della Sala F, Carbone L, Manna L, Maruccio G, Cingolani R, De Giorgi M (2008) Intrinsic optical nonlinearity in colloidal seeded grown CdSe/CdS nanostructures: photoinduced screening of the internal electric field. Phys Rev B 78(19):195313
83. Ranjan V, Allan G, Priester C, Delerue C (2003) Self-consistent calculations of the optical properties of GaN quantum dots. Phys Rev B 68(11):115305
84. Salviati G, Rossi F, Armani N, Grillo V, Martinez O, Vinattieri A, Damilano B, Matsuse A, Grandjean N (2004) Optical and structural characterization of self-organized stacked GaN/AlN quantum dots. J Phys: Condens Matter 16(2):S115–S126
85. Brown RH, Twiss RQ (1956) A test of a new type of stellar interferometer on Sirius. Nature 178:1046–1048
86. Kimble HJ, Dagenais M, Mandel L (1977) Photon antibunching in resonance fluorescence. Phys Rev Lett 39:691–695
87. Purcell EM (1976) The question of correlation between photons in coherent light rays. Nature 178:1449–1450
88. Pisanello F, Martiradonna L, Lemenager G, Spinicelli P, Fiore A, Manna L, Hermier JP, Cingolani R, Giacobino E, De Vittorio M, Bramati A (2010) Room temperature-dipolelike single photon source with a colloidal dot-in-rod. Appl Phys Lett 96(3):033101
89. Langbein W, Hetterich M, Klingshirn C (1995) Many-body effects and carrier dynamics in CdSe/CdS stark superlattices. Phys Rev B 51(15):9922–9929
90. Halsall MP, Nicholls JE, Davies JJ, Cockayne B, Wright PJ (1992) CdS/CdSe intrinsic stark superlattices. J Appl Phys 71(2):907–915
91. Sitt A, Della Sala F, Menagen G, Banin U (2009) Multiexciton engineering in seeded core/shell nanorods: transfer from type-I to quasi-type-II regimes. Nano Lett 9(10):3470–3476
92. Ashroft NW, Mermin ND (1976) Solid state physics. Brooks Cole, New York
93. Kreibig U (1974) Electronic properties of small silver particles: the optical constants and their temperature dependence. J Phys F 4:999–1014
94. Fiore A, Mastria R, Lupo MG, Lanzani G, Giannini C, Carlino E, Morello G, De Giorgi M, Li Y, Cingolani R, Manna L (2009) Tetrapod-shaped colloidal nanocrystals of II-VI semiconductors prepared by seeded growth. J Am Chem Soc 131(6):2274–2282
95. Martiradonna L, Carbone L, Tandaechanurat A, Kitamura M, Iwamoto S, Manna L, De Vittorio M, Cingolani R, Arakawa Y (2008) Two-dimensional photonic crystal resist membrane nanocavity embedding colloidal dot-in-a-rod nanocrystals. Nano Lett 8(1):260–264
96. Ahmed S, Ryan KM (2009) Centimetre scale assembly of vertically aligned and close packed semiconductor nanorods from solution . Chem Commun 42:6421–6423
97. Baranov D, Fiore A, van Huis M, Giannini C, Falqui A, Lafont U, Zandbergen H, Zanella M, Cingolani R, Manna L (2010) Assembly of colloidal semiconductor nanorods in solution by depletion attraction. Nano Lett 10(2):743–749
98. Rizzo A, Nobile C, Mazzeo M, De Giorgi M, Fiore A, Carbone L, Cingolani R, Manna L, Gigli G (2009) Polarized light emitting diode by long-range nanorod self-assembling on a water surface. ACS Nano 3(6):1506–1512
99. Htoon H, Hollingworth JA, Malko AV, Dickerson R, Klimov VI (2003) Light amplification in semiconductor nanocrystals: quantum rods versus quantum dots. Appl Phys Lett 82(26):4776–4778
100. Kazes M, Lewis DY, Ebenstein Y, Mokari T, Banin U (2002) Lasing from semiconductor quantum rods in a cylindrical microcavity. Adv Mater 14(4):317–321
101. Kazes M, Lewis DY, Banin U (2004) Method for preparation of semiconductor quantum-rod lasers in a cylindrical microcavity. Adv Funct Mater 14(10):957–962

102. Zavelani-Rossi M, Lupo MG, Krahne R, Manna L, Lanzani G (2010) Lasing in self-assembled microcavities of CdSe/CdS core/shell colloidal quantum rods. Nanoscale 2(6):931–935
103. Mie G (1908) Ann Physik 25:377–445
104. Deegan RD, Bakajin O, Dupont TF, Huber G, Nagel SR, Witten TA (1997) Capillary flow as the cause of ring stains from dried liquid drops. Nature 389(6653):827–829
105. Nobile C, Carbone L, Fiore A, Cingolani R, Manna L, Krahne R (2009) Self-assembly of highly fluorescent semiconductor nanorods into large scale smectic liquid crystal structures by coffee stain evaporation dynamics. J Phys Condens Matter 21(26):264013
106. Chin PTK, Donega CDM, Bavel SS, Meskers SCJ, Sommerdijk N, Janssen RAJ (2007) Highly luminescent CdTe/CdSe colloidal heteronanocrystals with temperature-dependent emission color. J Am Chem Soc 129(48):14880–14886
107. Jones M, Kumar S, Lo SS, Scholes GD (2008) Exciton trapping and recombination in type IICdSe/CdTe nanorod heterostructures. J Phys Chem C 112(14):5423–5431
108. Donega CDM (2010) Formation of nanoscale spatially indirect excitons: evolution of the type-II optical character of CdTe/CdSe heteronanocrystals. Phys Rev B 81(16):165303
109. Kim H, Achermann M, Balet LP, Hollingsworth JA, Klimov VI (2005) Synthesis and characterization of Co/CdSe core/shell nanocomposites: bifunctional magnetic-optical nanocrystals. J Am Chem Soc 127(2):544–546
110. Zanella M, Falqui A, Kudera S, Manna L, Casula MF, Parak WJ (2008) Growth of colloidal nanoparticles of group II-VI and IV-VI semiconductors on top of magnetic iron-platinum nanocrystals. J Mater Chem 18(36):4311–4317
111. He SL, Zhang HW, Delikanli S, Qin YL, Swihart MT, Zeng H (2009) Bifunctional magneto-optical FePt-CdS hybrid nanoparticles. J Phys Chem C 113(1):87–90
112. Gao JH, Zhang B, Gao Y, Pan Y, Zhang XX, Xu B (2007) Fluorescent magnetic nanocrystals by sequential addition of reagents in a one-pot reaction: a simple preparation for multifunctional nanostructures. J Am Chem Soc 129(39):11928–11935
113. Gu HW, Zheng RK, Zhang XX, Xu B (2004) Facile one-pot synthesis of bifunctional heterodimers of nanoparticles: a conjugate of quantum dot and magnetic nanoparticles. J Am Chem Soc 126(18):5664–5665
114. Kwon KW, Shim M (2005) Gamma-Fe2O3/II-VI sulfide nanocrystal heterojunctions. J Am Chem Soc 127(29):10269–10275
115. McDaniel H, Shim M (2009) Size and growth rate dependent structural diversification of Fe3O4/CdS anisotropic nanocrystal heterostructures. ACS Nano 3(2):434–440
116. Selvan ST, Patra PK, Ang CY, Ying JY (2007) Synthesis of silica-coated semiconductor and magnetic quantum dots and their use in the imaging of live cells. Angew ChemInt Edit 46(14):2448–2452
117. Habas SE, Yang PD, Mokari T (2008) Selective growth of metal and binary metal tips on CdS nanorods. J Am Chem Soc 130(11):3294–3295
118. Hosoki K, Tayagaki T, Yamamoto S, Matsuda K, Kanemitsu Y (2008) Direct and stepwise energy transfer from excitons to plasmons in close-packed metal and semiconductor nanoparticle monolayer films. Phys Rev Lett 100(20):207404
119. Nobile C, Fonoberov VA, Kudera S, Della Torre A, Ruffino A, Chilla G, Kipp T, Heitmann D, Manna L, Cingolani R, Balandin AA, Krahne R (2007) Confined optical phonon modes in aligned nanorod arrays detected by resonant inelastic light scattering. Nano Lett 7(2):476–479
120. Krahne R, Chilla G, Schuller C, Kudera S, Tari D, De Giorgi M, Heitmann D, Cingolani R, Manna L (2006) Shape dependence of the scattering processes of optical phonons in colloidal nanocrystals detected by Raman Spectroscopy. J Nanoelectr Optoelect 1(1):104–107
121. Becker K, Lupton JM, Muller J, Rogach AL, Talapin DV, Weller H, Feldmann J (2006) Electrical control of Forster energy transfer. Nat Mater 5(10):777–781
122. Zavelani-Rossi M, Krahne R, Della Valle G, Longhi S, Franchini IR, Girardo S, Scotognella F, Pisignano D, Manna L, Lanzani G, Tassone F (2012) Self-assembled CdSe/CdS nanorod micro-lasers fabricated from solution by capillary jet deposition. Laser Photonics Rev 6(5):678–683

http://www.springer.com/978-3-642-36429-7

Physical Properties of Nanorods

Krahne, R.; Manna, L.; Morello, G.; Figuerola, A.; George, C.; Deka, S.

2013, XVI, 282 p. 136 illus., 76 illus. in color., Hardcover
ISBN: 978-3-642-36429-7